Article

Effects of MacroH2A and H2A.Z on Nucleosome Dynamics as Elucidated by Molecular Dynamics Simulations

Samuel Bowerman[1] and Jeff Wereszczynski[1,*]
[1]Department of Physics and Center for Molecular Study of Condensed Soft Matter, Illinois Institute of Technology, Chicago, Illinois

ABSTRACT Eukaryotes tune the transcriptional activity of their genome by altering the nucleosome core particle through multiple chemical processes. In particular, replacement of the canonical H2A histone with the variants macroH2A and H2A.Z has been shown to affect DNA accessibility and nucleosome stability; however, the processes by which this occurs remain poorly understood. In this study, we elucidate the molecular mechanisms of these variants with an extensive molecular dynamics study of the canonical nucleosome along with three variant-containing structures: H2A.Z, macroH2A, and an H2A mutant with macroH2A-like L1 loops. Simulation results show that variant L1 loops play a pivotal role in stabilizing DNA binding to the octamer through direct interactions, core structural rearrangements, and altered allosteric networks in the nucleosome. All variants influence dynamics; however, macroH2A-like systems have the largest effect on energetics. In addition, we provide a comprehensive analysis of allosteric networks in the nucleosome and demonstrate that variants take advantage of stronger interactions between L1 loops to propagate dynamics throughout the complex. Furthermore, we show that posttranslational modifications are enriched at key locations in these networks. Taken together, these results provide, to our knowledge, new insights into the relationship between the structure, dynamics, and function of the nucleosome core particle and chromatin fibers, and how they are influenced by chromatin remodeling factors.

INTRODUCTION

Eukaryotes package their genetic code in highly ordered chromatin fibers. The fundamental unit of these structures is the nucleosome core particle (NCP), a complex of ~147 base pairs of DNA that are wrapped around eight histone proteins (Fig. 1) (1). Although they have minimal sequence homology, each core histone has a structural motif of an N-terminal tail, three helices connected by two loops (α1-L1- α2-L2- α3), and a C-terminal tail (1,2). In the assembled NCP, histones are structurally divided into a $(H3\text{-}H4)_2$ tetramer that is positioned between two H2A-H2B dimers. The only location of interdimer interactions is at the base of the NCP that is formed by the H2A L1 loops, whereas each dimer has two interfaces with the tetramer: the H2A docking domain (DD) and the H3-H4 four-helix bundle. (1-4)

Cells regulate chromatin stability and DNA accessibility by changing the biochemical properties of the NCP (5-8). One of the primary chromatin remodeling mechanisms is the replacement of H2A or H3 histones with histone variants. (9-15) These variants have a similar structure and sequence to the canonical histones; however, they diverge at key locations that affect interhistone and DNA-histone contacts. These differences alter the structure and stability of the NCP and are therefore implicated in modulating transcriptional activity. For example, the H2A variant macroH2A exists in large populations in the inactive X chromosome of females but is sparse in active genes (11,16,17). In contrast, the H2A.Z variant has been linked to both transcriptional activation and repression and is enhanced in regulatory regions of the genome such as promoters and enhancers (18,19).

Histone variants influence chromatin through diverse mechanisms and structure/function relationships. macroH2A is unique among variants in that it possesses multiple domains, including the histone domain, a 38-residue linker sequence, and a large macro-domain (3,20). On its own, the histone domain is sufficient for reducing transcriptional activity in vivo and increasing the stability of the nucleosome complex, even though the crystal structure of an NCP containing this domain shows that variant incorporation causes only minor NCP rearrangements (11,21). The primary sequence is ~65% identical to canonical H2A and differs largely from H2A in two important regions: the L1 loops and the docking domain. The canonical ^{38}NYAE^{41} L1 loop possesses a net negative charge, whereas in contrast the macroH2A L1 ^{38}HPKY^{41} sequence has a net positive charge and an increased hydrophobicity. Substitutions of the L1 loops in canonical H2A with a macroH2A sequence (the L1-mutant) creates nucleosomes with in vitro stabilities and in vivo enrichments that are nearly identical to NCPs containing the complete macroH2A histone domain (11,21). Therefore, the L1 loops appear to be pivotal in dictating macroH2A's abilities to affect intranucleosomal functions. Meanwhile, changes to the docking domains

Submitted July 27, 2015, and accepted for publication December 10, 2015.
*Correspondence: jwereszc@iit.edu
Editor: Lois Pollack

0006-3495/16/01/0327/11
http://dx.doi.org/10.1016/j.bpj.2015.12.015

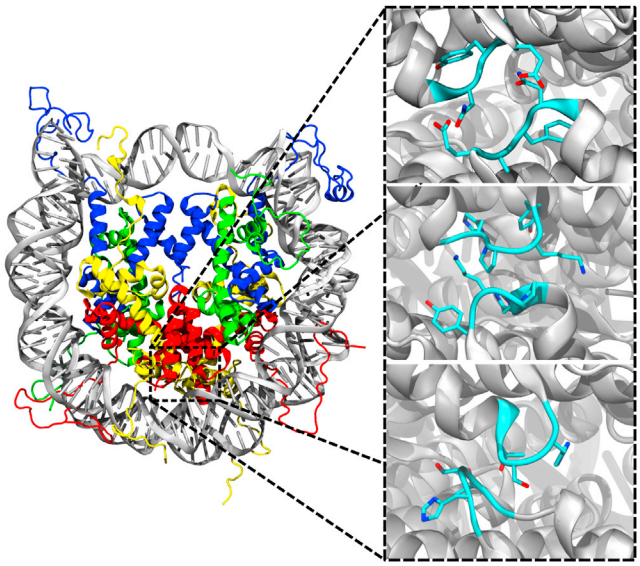

FIGURE 1 (*Left*) The nucleosome core particle: H3 (*blue*), H4 (*green*), H2A (*yellow*), H2B (*red*), and DNA (*gray*). (*Right*) The structures of the three L1 loop sequences considered in this study: canonical (*top*), macroH2A (*middle*), and H2A.Z (*bottom*). The canonical loops possess a net negative charge resulting from Glu^{41}, whereas the macroH2A loops possess a net positive charge from Lys^{40}. The L1 loops of H2A.Z are uncharged, but both macroH2A and H2A.Z loops introduce a larger hydrophobic volume than the canonical. To see this figure in color, go online.

show little effect on in vitro stability, but increase in vivo enrichment (11,21).

The role and mechanisms of the H2A.Z variant remains less well defined, with some experiments showing that H2A.Z increases NCP stability whereas others have found that it destabilizes the system. Similar to macroH2A, a comparison of the H2A.Z and canonical-containing NCP crystal structures show nearly identical overall conformations with the exception of two features (4). First, the structure of the L1 loops is altered, resulting in increased contacts between the two H2A/H2B dimers that likely helps to stabilize the histone octamer. Second, H2A.Z has fewer hydrogen bonds between the docking domain and H3, which could destabilize the dimer/tetramer interface. This combination of stabilizing one area of the NCP whereas destabilizing another may account for the disparate experimental results and the multiple functions H2A.Z appears to have (22).

Experiments have revealed a wealth of information about how histone variants affect NCP and chromatin function, but several questions still remain. For example, how do seemingly minor structural rearrangements affect the stability of the nucleosome? To what extent do changes in the L1 loops propagate through the complex? Do variants influence NCP function through only structural means, or do they take advantage of altered dynamics as well? To address these problems, we have performed extensive molecular dynamics (MD) simulations of four complete NCP systems that include 1) canonical H2A histones, 2) the macroH2A histone-fold domains, 3) L1-mutant H2A histones, and 4) H2A.Z histones. Our results indicate that different sequences in the L1 loops perturb the dynamic and energetic properties in this region of variant containing NCPs. These effects propagate throughout the complex and create subtle, yet important, rearrangements that alter the NCP structure and dynamics through both direct effects and modified allosteric networks. This allows histone variants to influence both the global dynamics and energetics of the NCP, and it likely contributes to large-scale structural changes such as DNA breathing and nucleosome opening, as well as inter-NCP interactions in chromatin fibers (23,24).

MATERIALS AND METHODS

System and simulation details

Simulations of the canonical-, macroH2A-, and H2A.Z-containing nucleosomes were initialized from their crystal structures (PDB: 1KX5, 1U35, and 1F66, respectively) (2-4). The L1-mutant structure was formed using the crystal structure of 1KX5, with the H2A L1 loops mutated from the canonical ^{38}NYAE^{41} to the macroH2A ^{38}HPKY^{41} sequence. The missing histone tail residues in the variant systems were constructed using 1KX5 as a model. To ensure that differences between system dynamics are purely results of H2A composition, non-H2A residues were mutated to match 1KX5. Furthermore, the 146 base pairs of DNA in the macroH2A and H2A.Z crystal structures were replaced with the 147 base pairs of 1KX5. Previous computational studies have suggested that H3, H4, and H2B orthologs have little effect on nucleosome stability (25), and comparative analysis of the crystal structures shows that variants do not significantly alter the DNA superhelical pathway (see Fig. S1 in the Supporting Material) (12). Further trajectory analysis confirms that these subtle changes to the variant systems have no discernible effect on the net system equilibration beyond noise (for further discussion and comparative analysis, see the Supporting Material).

The systems were neutralized and solvated in a TIP3P box of 150 mM NaCl that extended at least 10 Å from the solute, creating systems of ~250,000 atoms. Each system was simulated three times (see the Supporting Material for more details). The simulations were done in the NAMD engine (v2.9) using the AMBER12SB fixed point-charge force field (26,27). Monovalent ions were modeled according to Joung and Cheatham (28). Production simulations were done in the NPT ensemble using standard techniques (29-36). Coordinates were stored every 2 ps. Visualizations were made using VMD and PyMOL (37-39).

Allosteric pathways calculations

Allosteric effects were computed with multiple techniques (for specific details, see the Supporting Material). Per-residue differences in dynamics were determined by calculating the Kullback-Leibler (KL) divergence of dihedral angle populations (40). For these calculations, the canonical populations were used as a reference set. Spurious results were filtered using bootstrapping techniques. Residue-residue correlations were calculated by utilizing the largest mutual information method (41,42). Residue contacts were determined to be when protein C_α or nucleic C1′ atoms were within 10 Å in at least 70% of the configurations (43). The mapping of allosteric networks was conducted using the weighted implementation of suboptimal pathways (WISP) approach (44). The edge-betweenness centrality of residues in the optimal networks were calculated with the NetworkX Python package, with the significance determined by a hypergeometric distribution (see the Supporting Material) (45-47).

Interaction energies

Interaction energies between the two H2A histone L1 loops were calculated using cpptraj (48). A cutoff distance of 15 Å was used for both van der Waals and electrostatic interactions. Because the L1 loops interact with both protein and DNA, an intermediate dielectric value of 5 was considered ($\varepsilon_{DNA} = 8$, $\varepsilon_{protein} = 4$) (49,50). Hydrogen bonds were defined by a separation distance of 3.5 Å and an angle of 30°.

DNA binding and complex assembly energies were calculated using the MMPBSA.py function of AMBERTOOLS (v.14) (51). The level of theory was restricted to the generalized born implicit solvent (igb = 5, radii = mbondi2) (52). Coordinates from every 100 ps of production simulation were used. Although the superhelical form of DNA is highly irregular without histones (30), the octamer fold can form without the presence of DNA (53). Thus, to balance accuracy and computational efficiency, a hybrid two-trajectory molecular mechanics/generalized born surface area (MM/GBSA) approach was taken in which the coordinates for the protein constituents were extracted from the nucleosome simulations, but the unbound DNA coordinates were taken from a separate simulation of 147 bp of linear B-form DNA in a 150 mM NaCl environment (see the Supporting Materialsfor complete discussion). Error bars in the energies and all other measures were defined by the standard error of the mean, where the number of independent points was determined by the statistical inefficiency of the data set, as computed with the PyMBAR package (54).

RESULTS

We performed three independent 250 ns MD simulations for four complete NCP systems: 1) canonical, 2) macroH2A histone-fold, 3) L1-mutant, and 4) H2A.Z containing NCPs. In each set of simulations, ~50 ns was required for the root-mean square deviations (RMSDs) of the complexes to stabilize (Figs. S3–S6) and the tails to collapse from their initial elongated states, resulting in 200 ns of production time per simulation (600 ns per system). These results are consistent with previous MD simulations of the canonical NCP that demonstrated that the overall complex is stable on the hundreds of ns timescale and that the histone tails form strong interactions with the nucleosomal DNA (23,55,56). Comparisons between the canonical and variant systems demonstrate that variants have both subtle and large-scale effects on the structure and dynamics of the L1 loops, DNA-histone interactions, and allosteric networks throughout the NCP. Further comparison of our H2A.Z simulations with a control in which no substitutions were made to the 1F66 crystal structure demonstrated that the changes we introduced to match the 1KX5 structure did not significantly affect structural or dynamical properties beyond the equilibration period (see the Supporting Material for further details and discussion).

Altered dynamics of L1 loops

Modifications of the L1 loop sequences in histone variants alter their dynamics and energetics. In the canonical NCP simulations, an average of 0.5 hydrogen bonds were formed between the L1 loops, primarily between the carboxamide nitrogen of asparagine and the carboxylate group of the symmetric glutamate. This is consistent in the L1-mutant (~0.4) but is reduced to ~0.2 in macroH2A. In these two systems, the most prevalent hydrogen bonds were formed between the phenol oxygen of tyrosine and the hydrogen-free nitrogen of the symmetric histidine. In the H2A.Z simulations, L1-L1 hydrogen bonds were almost nonexistent (Table S1).

Although hydrogen bonds form most frequently in the canonical loops, the net L1 loop interaction energies are more favorable in the variants (Table 1). The close proximity of the negatively charged glutamates in the canonical NCP creates a disfavored electrostatic interaction. However, the L1-mutant and macroH2A systems avoid an analogous situation through Lys-DNA interactions, which separates the like-charges and creates a more favorable electrostatic configuration. Meanwhile, the lack of charge in the H2A.Z L1 loops also creates a more favorable electrostatic interaction than the canonical NCP. In addition, the L1 loop rearrangement in the macroH2A and L1-mutant systems is further stabilized by van der Waals interactions. In total, the interaction energies of the L1 loops in the L1-mutant and macroH2A structures are substantially favored over those of the canonical ΔU_{total} values of -11.2 ± 2.4 and -8.6 ± 2.3 kcal/mol. The H2A.Z L1 loop conformations are also more favorable than in the canonical system ($U_{total} = -4.4 \pm 2.3$ kcal/mol).

The different net charges of the L1 loops influence their interactions with the nucleosomal DNA. In the canonical L1 loops, the negative charge located on Glu^{41} causes a repulsive force to the negatively charged DNA. However, in the macroH2A and L1-mutant systems, Lys^{40} introduces a positive charge into the loop that forms a salt bridge with the DNA base pair across the axis of symmetry (Fig. 2). The lysine forming this salt bridge sterically hinders the symmetric lysine residue from doing the same, so the interaction exists in only one dimer. The noninteracting lysine is primarily exposed to solvent while intermittently forming a hydrogen bond with a neighboring

TABLE 1 Net Interaction Energies between the H2A L1 Loops Show that macroH2A and H2A.Z Loops Have More Favorable Interactions than Canonical L1 Loops

System	U_{elect}	U_{vdW}	U_{tot}	U_{elect}	U_{vdW}	U_{tot}
Canonical NCP	6.3 ± 2.0	−9.4 ± 0.8	−3.1 ± 2.2	–	–	–
L1-mutant	−0.9 ± 0.4	−13.4 ± 0.8	−14.3 ± 0.9	−7.2 ± 2.0	−4.0 ± 0.8	−11.2 ± 2.4
MacroH2A NCP	0.4 ± 1.1	−12.1 ± 0.9	−11.7 ± 1.0	−5.9 ± 2.3	−2.7 ± 0.9	−8.6 ± 2.3
H2A.Z NCP	−0.6 ± 0.1	−6.9 ± 0.6	−7.5 ± 0.6	−6.9 ± 2.0	2.4 ± 1.0	−4.4 ± 2.3

U is defined as the difference in energies between each variant and the canonical system. Negative values show favorability in the variants. All values are reported in kcal/mol.

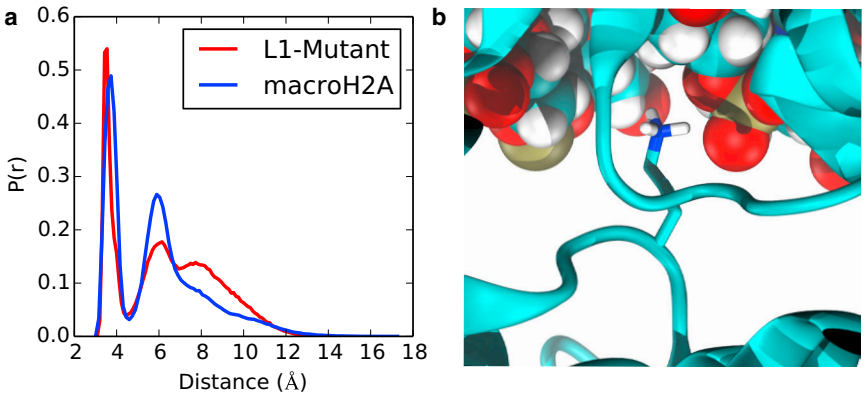

FIGURE 2 (*a*) Distance populations for Lys[40] to DNA phosphate show an interaction that is unique to macroH2A-like L1 loops. (*b*) A representative configuration of the Lys side chain stretching across the molecule to interact with the dimer's nonassociated DNA. This orientation sterically hinders the symmetric loop from forming a similar interaction. This interaction contributes significantly to stabilizing DNA-octamer binding in the macroH2A and L1-mutant systems. To see this figure in color, go online.

histidine. Because the L1 loops of H2A.Z are uncharged, they are not capable of forming similar interactions, and therefore did not make any direct contacts with the DNA. Taken with the results of the L1-L1 loop dynamics, we observe that the macroH2A-like loop sequences stabilize both protein-protein and protein-DNA interactions when compared with both the canonical and H2A.Z histones.

Variant presence alters dimer orientations

Reorganization of the L1-loops creates perturbations that affect the dimer orientations in the NCP. For example, the H2A α2 helix extends across the dimer, with its N-terminal (the base) at the L1-interface and its C-terminal (the top) solvent-exposed on the far side of the molecule (Fig. 3). Simulation analysis showed that the canonical system exhibited a separation of 67.1 $\pm$ 0.2 Å between the tops, and 34.8 $\pm$ 0.1 Å between the bottoms of the H2A α2 helices. In contrast, in each of the variant NCPs there is a bulging motion in which the base separation is increased to ~36.5 Å while the top separation is decreased to ~66.1 Å. Although these changes in orientation are only on the order of an Å, a *t*-test indicated that they are all extremely statistically significant (Fig. 3).

This subtle reorientation of the dimers alters histone-DNA hydrogen bonding. For example, the guanidine group of H2A Arg[29] forms a hydrogen bond with the phosphate group of the 23rd base pair of DNA in all systems. In the canonical NCP, this bond forms in 63% of the configurations, whereas in the L1-mutant it is formed 70% of the time. In addition, the frequency of hydrogen bonding between the 22nd base pair phosphate and the backbone amide of H2B Ser[33] increases from 50% in the canonical system to 60% in the L1-mutant structure. In H2A.Z, the hydrogen bonding at these locations increases drastically to 73% and 85%, respectively. Interestingly, the macroH2A nucleosome shows a decreased frequency of both of these interactions (52% and 30%, respectively). The reduced hydrogen bonding in the macroH2A nucleosome is likely a result of sequence deviations in the nearby H2A 1 helix (canonical: ^{30}VH^{31}, H2A.Z: ^{30}IH^{31}, macro: ^{30}ML^{31}).

The dimer realignment also affects the hydrogen bonding between protein constituents in the histone core. In the canonical NCP, an average of 14.8 hydrogen bonds are formed between a single dimer and the tetramer, which is in agreement with the ~15 observed in the crystal structure. This increases to an average of 16.5 in the L1-mutant. The macroH2A and H2A.Z nucleosomes display an average of 14.7 and 13.8 hydrogen bonds, which are substantially more frequent than the ~8 observed in the initial configurations. This increase in hydrogen bonding is a result of dimer reorientation, which increases the interaction between residues in the four-helix bundle.

Histone H2A L1 sequence influences dynamics throughout the nucleosome

The L1 loops not only influence dimer reorientation, but they also perturb the local dynamics of residues throughout the nucleosome. Calculations of the KL divergence between the canonical and variant systems showed the expected disparity in dihedral sampling of residues within the L1 loop region (Fig. 4). However, they also highlighted significant changes in the dynamics of residues that are distant from these loops. In both the L1-mutant and macroH2A systems, the dimer and tetramer constituents of the docking domains have statistically significant KL divergence values, indicating that their local dynamics are different in these systems relative to the canonical NCP. Although this was expected in the macroH2A and H2A.Z systems because of their sequence deviations, the L1-mutant is sequentially identical to the canonical system in these areas. Therefore, the observed difference in dynamics must be because of allosteric networks that are shifted by the L1 mutation. On the other hand, the dynamics in the histone core of H2A.Z only show small differences from the canonical system, most notably along the H2B α2 helix, whereas the largest divergences are in the DNA.

The L1-mutant and macroH2A variants also have increased dynamical correlations between the H2A L1 loops

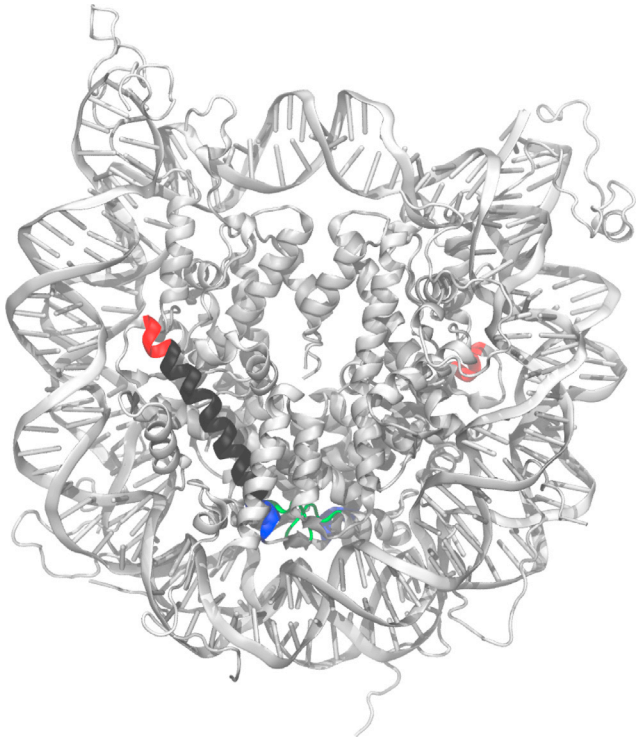

System	top	bottom
Canonical NCP	67.1 ± .2	34.8 ± .1
L1-Mutant	66.0 ± .2	36.8 ± .4
p-value	.0003	.0001
macroH2A NCP	66.2 ± .3	36.2 ± .1
p-value	.0001	.0001
H2A.Z NCP	66.0 ± .1	36.1 ± .1
p-value	.0001	.0001

FIGURE 3 Separation distances for H2A α2 helix locations show a bulging effect in histone variants. The helix is displayed in black whereas the helix top is highlighted in red and the bottom in blue. The L1-loops are shown in green for clarity. Shifts in mean separation are on the order of an Å, but the changes in populations are all incredibly significant. To see this figure in color, go online.

and key portions of the NCP (Table 2; Fig. S9). The strengthened interactions in the L1 loops increase the L1-L1′ correlations from 0.42 in the canonical system to >0.67 in each of the variants. In both the canonical and H2A.Z systems, the average correlation between the L1 loops and either docking domain (symmetric: DD, opposing dimer: DD′) was 0.36 to 0.38. However, in the L1-mutant the average L1-DD and L1-DD′ correlations increased to 0.51 for both measurements, which were further increased to 0.56 and 0.60 in the macroH2A structure. Although the variants had an increased correlation between the L1 loops and DNA near the base of the nucleosome, the correlations between the L1 loops and DNA extremities were similar in all four systems.

Variant presence alters allosteric pathways

The origins of the altered dynamics and correlations in NCPs with variants were probed by computing the optimal and suboptimal correlation pathways using with the WISP algorithm (44). Allosteric networks were calculated between the L1 loops and the DNA entry and exit sites, and the tetramer components of the docking domains for each system. The results revealed that not only are there several networks of dynamically coupled residues in the canonical NCP, but that these networks are both modified and strengthened by macroH2A, H2A.Z, and the L1-mutant. The shifts are because of both changes in the NCP hydrogen bonding networks from subtle repositioning of the H2A histones, as well as increased interactions of the L1 loops with one another and with the nucleosomal DNA.

In the L1-to-symmetric-DNA-end pathways, the canonical system utilizes three main routes for information transfer (Fig. 5). In the first, networks primarily pass through neighboring H2B Ser^{33}-DNA and H2A α1 helix Arg^{29}-DNA hydrogen bond interactions and into the DNA, whereas in the second the networks enter the DNA through the H2A Arg^{42}-DNA hydrogen bond near the intradimer interaction site. The third route for propagation extends along the H2A α2 helix, which passes dynamic information into the DNA base pairs via a Thr^{76}-DNA interaction. The pathways of H2A.Z are similar to the canonical but with more pathways accessing the H2A α1 Arg^{29}-DNA interaction than that of H2B Ser^{33}-DNA. In the L1-mutant, the increased prevalence of the Arg^{29}-DNA hydrogen bond heavily biases information transfer through this network and increases the strength of this pathway. The decreased Arg^{29}-DNA interaction in the macroH2A nucleosome causes information to be transferred primarily via the H2A Arg^{42}-DNA hydrogen bond, with a significant number of pathways also traversing the H2A α2 helix.

The effects of L1-L1′ communication transfer are most apparent in the networks between an L1 loop and the DNA end of the opposite symmetry. In the canonical nucleosome, there exist no pathways between L1 loops, therefore networks must pass through indirect routes that include the DNA and histone tails. However, in all of the variant structures information is readily exchanged between the L1 loops, allowing the pathways to immediately cross into the opposite symmetry dimer (Figs. S14–S17). Once information is passed into this dimer, it follows the typical pathways for L1-to-symmetric-DNA-end propagation. This results in allosteric networks that are not only stronger, but more direct in the histone variants.

Pathways between the L1 loop and docking domains in the same dimer are similar in all systems, but there is a large disparity in the pathways between L1 loops and the docking domain of the other dimer constituent. In the canonical NCP, the majority of paths pass from the L1 loops through the H2B α2 helix into the tetramer

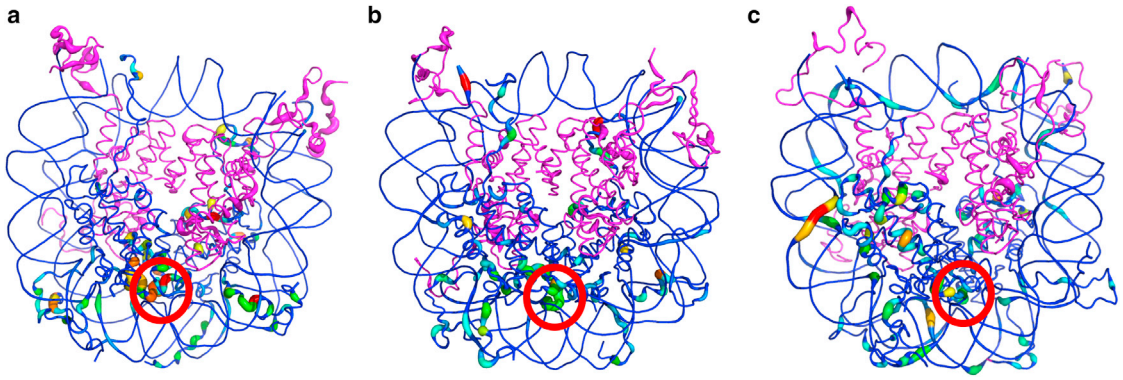

FIGURE 4 Per-residue Kullback-Leibler divergence values for difference in sampled dihedral angles for the (*a*) L1-mutant, (*b*) macroH2A, and (*c*) H2A.Z nucleosomes, referenced against populations from the canonical system. The dimers and DNA residues are represented in a rainbow spectrum. Narrow and blue regions display similar dynamics to the canonical nucleosome, and regions displaying larger divergence values are wider and increase from blue to green to red. The tetramer is shown in magenta, where the tube radius is wider for residues with larger deviations from canonical-like dynamics. Divergence values are large near the L1-L1 interface (*red circle*), but significant differences are also observed in faraway regions. To see this figure in color, go online.

portion of the docking domain via the four helix bundle of H2B-H4. The L1-mutant structure shows an increased number of contacts in this region, creating a more diverse set of pathways between bundle helices. The macroH2A nucleosome displays an alternate route in which pathways instead access the docking domain region via protein-DNA interactions. The H2A.Z system uniquely passes information along the H2B α2 helix of the opposing dimer. Pathways in H2A.Z also access the protein-DNA type route of macroH2A and the four helix bundle route of the canonical and L1-mutant systems, but at a reduced frequency.

PTM locations are enriched at allosteric hotspots

Beyond these specific pathways, dynamic networks exist throughout the NCP. To discern the importance of individual residues on these global networks, the edge-betweenness centrality of nucleosome residues was computed (Fig. S10) (46). In the canonical NCP, a majority of the optimal pathways rely heavily on the DNA base pairs and neighboring histone tail lysine and arginine residues to propagate communication throughout the system. In H2A.Z, an increased number of shortest pathways access the L1 loops and the H4 α2 helix, but there remains a heavy reliance on the DNA and histone tails. In the L1-mutant and macroH2A nucleosomes, dynamic traffic to the four-helix bundle increases. Furthermore, pathways in these systems access L1 residues more frequently than any other region.

TABLE 2 Average Correlations between L1 Loops and Relevant Regions of the Nucleosome Core Particle for Each System

System	L1-L1′	L1-DD	L1-DD′	L1-DNA
Canonical NCP	0.42	0.38	0.36	0.49
L1-mutant	0.70	0.51	0.51	0.48
MacroH2A NCP	0.73	0.56	0.60	0.48
H2A.Z NCP	0.67	0.38	0.38	0.44

The L1-L1′ and L1-DD(′) correlations are significantly stronger in the systems possessing the macroH2A L1 loops, whereas L1 correlations to the DNA extremities are unchanged. The associated docking domain is abbreviated as DD, and the docking domain of the opposing dimer is abbreviated as DD′.

Interestingly, we find that residues with the highest edge-betweenness scores are more likely to be the sites of posttranslational modifications (PTMs). Based on the distribution of centrality scores, we classify residues in the upper 10th percentile as hotspots for communication (see the Supporting Material). A comparison of known PTM sites with these allosteric hotspots indicates that PTMs are enriched at these locations, with an enrichment factor of 254% (p-value of 0.0155). When we compare our hot spot analysis with known PTM sites (7,57,58), we observe a significant population of PTM targets (Fig. 6). Although PTMs in the histone core are identified more frequently than those in the tails, the most significant subset contains PTMs that have been implicated in affecting mononucleosome stabilities (monoNCP PTMs) (7). In relation to the types of PTMs, methylation sites are linked with allosteric hotspots more frequently than phosphorylations or acetylations, likely because of their presence at DNA entry/exit sites and between turns of superhelical DNA.

An overall correlation between allosteric hotspots and PTM locations is maintained in the nucleosome variants; however, the specific details differ between the systems (Table S2). For example, all four systems show the importance of PTM sites in the H3 histone near the DNA extremities, whereas histone H4 monoNCP PTM sites in the four-helix bundle are accessed more frequently in variant networks. In general, the canonical system displays the greatest reliance on monoNCP PTMs, then the H2A.Z nucleosome, and finally the L1-mutant and macroH2A systems, respectively.

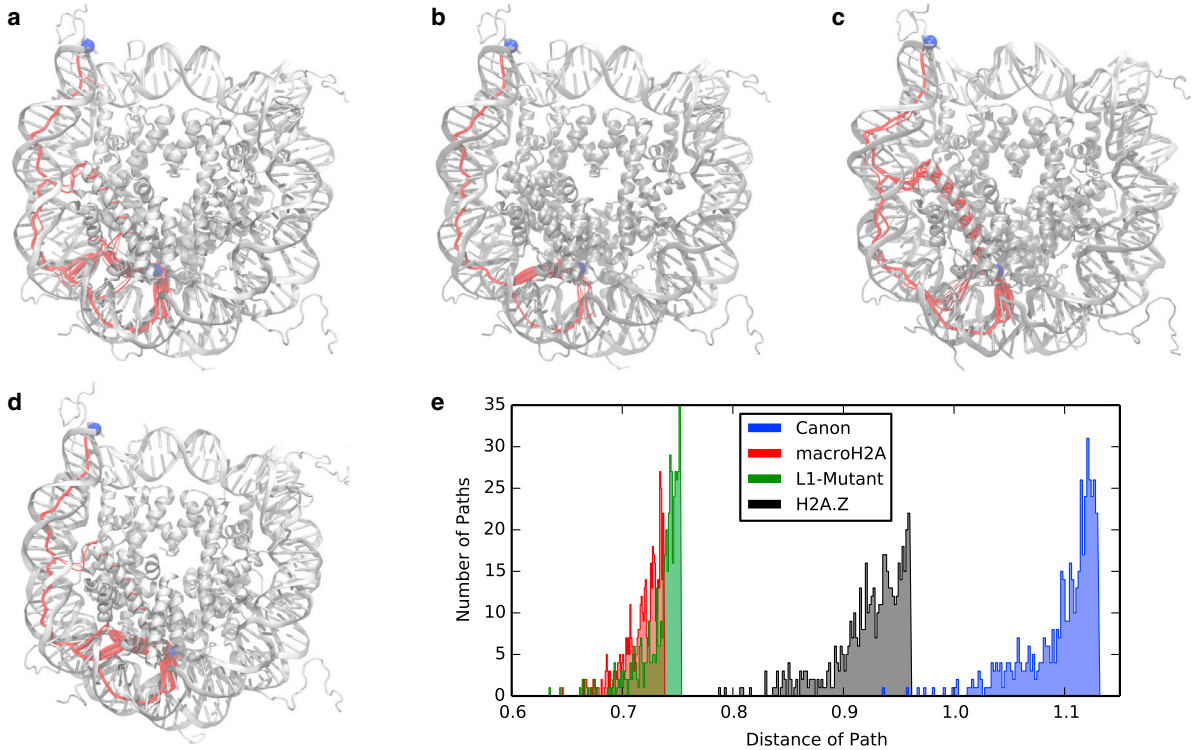

FIGURE 5 The 500 suboptimal pathways between the L1 loops and symmetrically associated DNA entry for the (*a*) canonical NCP, (*b*) L1-mutant, (*c*) macroH2A, and (*d*) H2A.Z projected on simulation snapshots. Also shown is the histogram of pathway distances (*e*). The L1 and DNA sites are represented as blue spheres, and the pathways are outlined in red with the wider pathways representing those of shorter distance. Pathways in the variants are shorter, and thus stronger, than in the canonical NCP. To see this figure in color, go online.

Structural stability in variant nucleosomes

To quantify global NCP dynamics, a full correlation analysis (FCA) was performed on the C atoms of the histone core α-helices (59). Two of the dominant motions identified in this analysis corresponded to the nucleosome opening motions described by Böhm et al. (24). Projections into the phase-space described by these and other FCA modes showed that all nucleosome systems had similar global dynamics on the hundreds of nanoseconds timescale (see Fig. S7). However, given that the dynamics of nucleosome opening likely occur on the millisecond timescale, our simulations are far too short to effectively explore the effects of histone variants on large-scale NCP dynamics.

In contrast to the nucleosome opening motions, the DNA end-to-end separation distance does depend on the identity

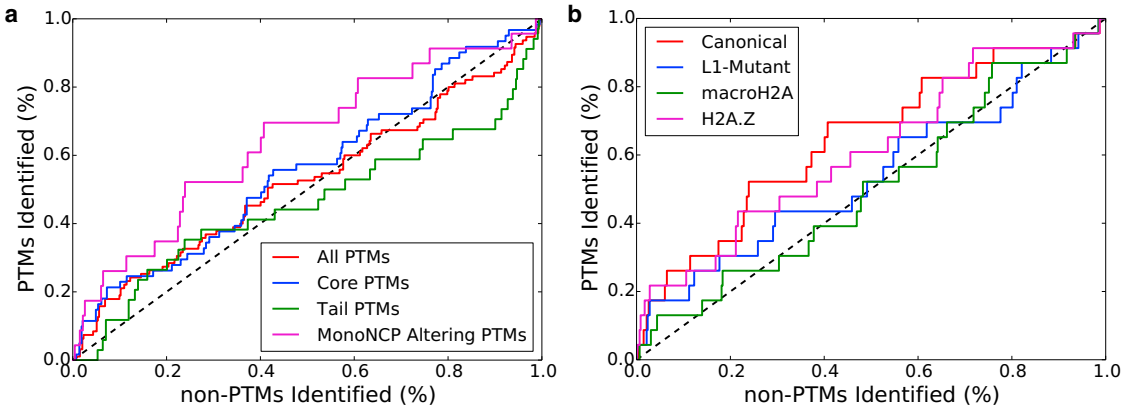

FIGURE 6 (*a*) Receiver operator curves (ROC) for subsets of PTM sites in the canonical nucleosome as identified by edge-betweenness centrality ranking. The largest enrichment can be seen in the PTM subset of monoNCP altering PTMs. The core PTMs are also more frequently identified than the tails. (*b*) ROC for monoNCP altering PTMs across the variant systems. The canonical and H2A.Z systems are shown to depend greater on monoNCP altering PTMs than the L1-mutant and macroH2A systems for distributing dynamic information. To see this figure in color, go online.

of the H2A histone (Fig. 7). This distance was defined as the separation between the center of masses of the innermost terminal nucleotide of each extremity, which were well behaved and displayed no base flipping. The sampling in the canonical system can be divided into two states: the prominent compact state centered at ~67 Å and the open state centered at 71 Å. The L1-mutant sampled both the open and closed states; however, the percentage of time spent in the open state was reduced from 14% to 11% of the simulation. Both the macroH2A and H2A.Z systems only sampled the closed state.

Results of an MM/GBSA analysis indicate that the overall DNA binding energetics are also altered by H2A variants. The DNA binding affinities to the L1-mutant and macroH2A octamers were 31.0 ± 9.1 and 5.7 ± 9.7 kcal/mol more favorable than binding to the canonical NCP (Table 3). There are two primary contributors to this shift: direct interactions with the L1 loops ($\Delta\Delta G_{L1}$) and the changes in the DNA configuration ($\Delta\Delta G_{DNA}$). In the L1-mutant and macroH2A systems, $\Delta\Delta G_{L1}$ was largely a result of removing the negatively charged Glu^{41} from the canonical loop and introduction of the Lys^{40}-DNA interaction, which combine for an increase in binding free energy on the order of 10 kcal/mol. The reorientation of the dimers in the macroH2A-like systems also influences a favorable shift in DNA conformation relative to the canonical system ($\Delta\Delta G_{DNA} = -9.3 \pm 5.6$ and -17.0 ± 1.8 kcal/mol for the L1-mutant and macroH2A nucleosomes, respectively). However, in macroH2A a number of small shifts in the remainder of the NCP oppose binding and therefore make it more comparable with the canonical system, which does not occur in the L1-mutant NCP. The H2A.Z nucleosome does not exhibit the same favorability for DNA binding when compared with the canonical octamer, but instead shows a disfavoring shift of 5.6 ± 8.9 kcal/mol. The removal of the negative charge on Glu^{41} creates a favorable shift of 5.8 ± 0.1 kcal/mol in $\Delta\Delta G_{L1}$, but this is balanced by the nearly identical free energy penalty in the DNA rearrangement term $\Delta\Delta G_{DNA}$.

Similarly, another MM/GBSA analysis revealed that macroH2A variants modify the energetics of complex assembly. The $\Delta G_{assembly}$ of the L1-mutant and macroH2A nucleosomes were -60.0 ± 9.5 and -18.5 ± 9.8 kcal/mol more favorable than the canonical system. The favorability in the macroH2A-like systems is a result of favorable DNA binding coupled with stronger protein-protein interactions. Calculations for $\Delta\Delta G_{assembly}$ of H2A.Z agree with previous calculations on a static NCP structure that suggested this complex is slightly less stable than the canonical nucleosome (25); however, our study builds off the results of Vijayalakshmi et al. by demonstrating that dynamic rearrangements bring the stabilities of these systems closer into agreement (Table 3).

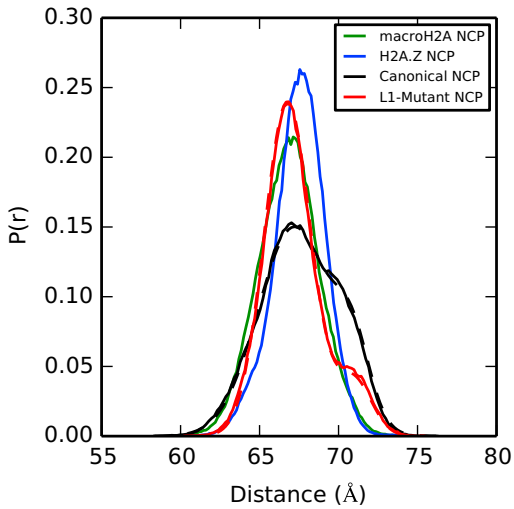

FIGURE 7 Distance populations for DNA end-to-end spread. The canonical system exists in two states: one centered around 67 Å (compact) and one centered around 71 Å (open). Although the L1-mutant samples both states, the amount of time spent in the open state is drastically reduced. The macroH2A and H2A.Z nucleosomes exist only in the compact state. Fits are represented in dotted lines. To see this figure in color, go online.

DISCUSSION

The simulations and analysis presented in this study detail a series of mechanisms by which the histone variants macroH2A and H2A.Z influence the dynamics of the nucleosome core particle. The subtle structural rearrangements these variants cause leverage the tightly packed nature of the histone core to influence the global energetics and dynamics of the complex, thus influencing gene expression. Dynamic effects appear to be particularly important, as they allow for the propagation of information through allosteric networks that span large distances. Although our simulations are only able to probe the sub-μs timescale, the dynamic differences observed at the dimer-tetramer and DNA/histone interfaces will likely be amplified on the ms timescale and result in these variants having altered nucleosome opening and DNA breathing motions.

These results also offer, to our knowledge, new insights into biochemical experiments that probed the mechanism of macroH2A. For example, Nusinow et al. showed that the L1-mutant is enriched in the inactive female X chromosome at nearly the same rate as the complete histone-domain of macroH2A (11). Point mutations demonstrated that enrichment was significantly increased by the two mutations that introduce additional bulk into the L1 loops, N38H and E41Y, whereas it was decreased by the Y39P mutation, which decreases the size of the L1 loop. Based on our results, we believe that larger side chains may help encourage the α2 bulging motion observed in each of the variant simulations, and therefore make the NCP more variant-like.

In another set of experiments, Chakravarthy et al. demonstrated that mutations to the L1 loops modulate the

TABLE 3 MM/GBSA Calculated Binding Energies for DNA Binding Affinity to the Histone Core in Each of the NCP Systems

System	$\Delta G_{binding}$	$\Delta\Delta G_{binding}$	$\Delta\Delta G_{L1}$	$\Delta\Delta G_{DNA}$	$\Delta G_{assembly}$	$\Delta\Delta G_{assembly}$
Canonical NCP	−428.6 ± 5.6	–	–	–	−618.6 ± 5.8	–
L1-mutant	−459.6 ± 7.2	−31.0 ± 9.1	−8.7 ± 0.1	−9.3 ± 5.6	−679.6 ± 7.5	−60.0 ± 9.5
MacroH2A NCP	−434.5 ± 7.9	−5.7 ± 9.7	−10.7 ± 0.1	−17.0 ± 1.8	−637.1 ± 7.9	−18.5 ± 9.8
H2A.Z NCP	−423.0 ± 6.9	5.6 ± 8.9	−5.8 ± 0.1	5.8 ± 5.4	−616.3 ± 6.9	2.3 ± 9.0

$\Delta\Delta G$'s are referenced against the canonical NCP. The L1 loop sequence and DNA conformations of the variant structures contribute significantly toward favorable binding of DNA in the macroH2A-like systems, relative the canonical NCP. All values are reported in kcal/mol.

salt-dependent stability of the histone octamer (21). They showed that in both the L1-mutant and macroH2A-containing system, the histone octamer is stable down to 0.5 M NaCl, whereas the canonical and H2A.Z-containing structures dissociate into dimer and tetramer constituents in solutions below 1.1 M. In agreement with this, we observe a significantly more favorable interaction between the H2A L1 loops in the variant structures than in the canonical structure. Because the L1-L1 interface is the only location of dimer-dimer interaction, stability in this region translates to octamer stability.

The mechanisms of H2A.Z remain more elusive. Stability studies have been nonconclusive as some indicate that H2A.Z enhances stability (60), whereas others suggest that it destabilizes the nucleosome (25). Our simulations show H2A.Z nucleosome stabilities that are in agreement with the canonical system, despite their differing dynamics. These systems were constructed with identical sequences, except for H2A composition. Therefore, our findings support a mechanism that suggests that H2A.Z by itself has little-to-no effect on NCP stability. Instead, H2A.Z presence may be combined with other factors, such as PTMs or H3 variant presence, to alter particle stability (22,61). Furthermore, the altered dynamics and locations of allosteric networks and hotspots between H2A.Z and canonical nucleosomes may result in different responses to these chromatin remodeling factors. The dimer reordering may also act to recruit transcriptional machinery to chromatin possessing large populations of H2A.Z, such as transcriptional starting sites.

Finally, we present a comprehensive analysis of the dynamic networks in the nucleosome. We observe that these networks are strongly affected by the dynamics of the L1 loops that are allosterically linked to a wide number of important regions in the nucleosome core. Using only small changes in their structure, variants are able to modify these networks to affect the function of the NCP. We hypothesize that this is a general mechanism that other chromatin remodeling factors may also utilize. For example, the finding that PTMs are enriched at residues with increased allosteric activity suggests that these perturbations may take advantage of dynamic networks to amplify their effects on chromatin and influence global NCP dynamics. In addition, by altering these networks, variants may be able to tune the responses of nucleosomes to specific PTMs. Future work to study the disparate effects of chromatin remodeling factors on dynamics in the nucleosome is required to fully understand the mechanisms of in vivo gene expression and regulation.

SUPPORTING MATERIAL

Supporting Materials and Methods, twenty-five figures, and two tables are available at http://www.biophysj.org/biophysj/supplemental/S0006-3495(15)04756-6.

AUTHOR CONTRIBUTIONS

S.B. performed the simulations. S.B. and J.W. designed the experiments, analyzed data, and wrote the manuscript.

ACKNOWLEDGMENTS

The authors thank S. Chakravarthy for valuable discussions concerning the work in this study.

This research was supported by the National Institute of General Medical Sciences of the National Institutes of Health (Grant No. R15GM114758). The content is solely the responsibility of the authors and does not necessarily represent the official views of the National Institutes of Health. This work used the Extreme Science and Engineering Discovery Environment (XSEDE), which is supported by National Science Foundation Grant No. ACI-1053575. In addition, this research used resources of the National Energy Research Scientific Computing Center, which is supported by the Office of Science of the U.S. Department of Energy under Contract No. DE-AC02-05CH11231.

REFERENCES

1. Luger, K., A. W. Mäder, …, T. J. Richmond. 1997. Crystal structure of the nucleosome core particle at 2.8 A resolution. *Nature.* 389:251–260.
2. Davey, C. A., D. F. Sargent, …, T. J. Richmond. 2002. Solvent mediated interactions in the structure of the nucleosome core particle at 1.9 a resolution. *J. Mol. Biol.* 319:1097–1113.
3. Chakravarthy, S., S. K. Gundimella, …, K. Luger. 2005. Structural characterization of the histone variant macroH2A. *Mol. Cell. Biol.* 25:7616–7624.
4. Suto, R. K., M. J. Clarkson, …, K. Luger. 2000. Crystal structure of a nucleosome core particle containing the variant histone H2A.Z. *Nat. Struct. Mol. Biol.* 7:1121–1124.
5. Osley, M. A., A. B. Fleming, and C. F. Kao. 2006. Histone ubiquitylation and the regulation of transcription. *Results Probl. Cell Differ.* 41:47–75.
6. Luger, K., M. L. Dechassa, and D. J. Tremethick. 2012. New insights into nucleosome and chromatin structure: an ordered state or a disordered affair? *Nat. Rev. Mol. Cell Biol.* 13:436–447.

7. Bowman, G. D., and M. G. Poirier. 2015. Post-translational modifications of histones that influence nucleosome dynamics. *Chem. Rev.* 115:2274–2295.
8. Zhang, Y., and D. Reinberg. 2001. Transcription regulation by histone methylation: interplay between different covalent modifications of the core histone tails. *Genes Dev.* 15:2343–2360.
9. Bönisch, C., and S. B. Hake. 2012. Histone H2A variants in nucleosomes and chromatin: more or less stable? *Nucleic Acids Res.* 40:10719–10741.
10. Shaytan, A. K., D. Landsman, and A. R. Panchenko. 2015. Nucleosome adaptability conferred by sequence and structural variations in histone H2A-H2B dimers. *Curr. Opin. Struct. Biol.* 32:48–57.
11. Nusinow, D. A., J. A. Sharp, …, B. Panning. 2007. The histone domain of macroH2A1 contains several dispersed elements that are each sufficient to direct enrichment on the inactive X chromosome. *J. Mol. Biol.* 371:11–18.
12. Chakravarthy, S., Y. Bao, …, K. Luger. 2004. Structural characterization of histone H2A variants. *Cold Spring Harb. Symp. Quant. Biol.* 69:227–234.
13. Pehrson, J. R., and V. A. Fried. 1992. MacroH2A, a core histone containing a large nonhistone region. *Science.* 257:1398–1400.
14. Choo, J. H., J. D. Kim, …, J. Kim. 2006. Allele-specific deposition of macroH2A1 in imprinting control regions. *Hum. Mol. Genet.* 15: 717–724.
15. Buschbeck, M., I. Uribesalgo, …, L. Di Croce. 2009. The histone variant macroH2A is an epigenetic regulator of key developmental genes. *Nat. Struct. Mol. Biol.* 16:1074–1079.
16. Chadwick, B. P., and H. F. Willard. 2002. Cell cycle-dependent localization of macroH2A in chromatin of the inactive X chromosome. *J. Cell Biol.* 157:1113–1123.
17. Costanzi, C., P. Stein, …, J. R. Pehrson. 2000. Histone macroH2A1 is concentrated in the inactive X chromosome of female preimplantation mouse embryos. *Development.* 127:2283–2289.
18. Guillemette, B., A. R. Bataille, …, L. Gaudreau. 2005. Variant histone H2A.Z is globally localized to the promoters of inactive yeast genes and regulates nucleosome positioning. *PLoS Biol.* 3:e384.
19. Abbott, D. W., V. S. Ivanova, …, J. Ausió. 2001. Characterization of the stability and folding of H2A.Z chromatin particles: implications for transcriptional activation. *J. Biol. Chem.* 276:41945–41949.
20. Chakravarthy, S., A. Patel, and G. D. Bowman. 2012. The basic linker of macroH2A stabilizes DNA at the entry/exit site of the nucleosome. *Nucleic Acids Res.* 40:8285–8295.
21. Chakravarthy, S., and K. Luger. 2006. The histone variant macro-H2A preferentially forms "hybrid nucleosomes.". *J. Biol. Chem.* 281:25522–25531.
22. Marques, M., L. Laflamme, …, L. Gaudreau. 2010. Reconciling the positive and negative roles of histone H2A.Z in gene transcription. *Epigenetics.* 5:267–272.
23. Roccatano, D., A. Barthel, and M. Zacharias. 2007. Structural flexibility of the nucleosome core particle at atomic resolution studied by molecular dynamics simulation. *Biopolymers.* 85:407–421.
24. Böhm, V., A. R. Hieb, …, J. Langowski. 2011. Nucleosome accessibility governed by the dimer/tetramer interface. *Nucleic Acids Res.* 39:3093–3102.
25. Vijayalakshmi, M., G. V. Shivashankar, and R. Sowdhamini. 2007. Simulations of SIN mutations and histone variants in human nucleosomes reveal altered protein-DNA and core histone interactions. *J. Biomol. Struct. Dyn.* 25:207–218.
26. Hornak, V., R. Abel, …, C. Simmerling. 2006. Comparison of multiple Amber force fields and development of improved protein backbone parameters. *Proteins.* 65:712–725.
27. Phillips, J. C., R. Braun, …, K. Schulten. 2005. Scalable molecular dynamics with NAMD. *J. Comput. Chem.* 26:1781–1802.
28. Joung, I. S., and T. E. Cheatham, 3rd. 2009. Molecular dynamics simulations of the dynamic and energetic properties of alkali and halide ions using water-model-specific ion parameters. *J. Phys. Chem. B.* 113:13279–13290.
29. Ryckaert, J.-P., G. Ciccotti, and H. J. Berendsen. 1977. Numerical integration of the cartesian equations of motion of a system with constraints: molecular dynamics of *n*-alkanes. *J. Comput. Phys.* 23: 327–341.
30. Bishop, T. C. 2005. Molecular dynamics simulations of a nucleosome and free DNA. *J. Biomol. Struct. Dyn.* 22:673–686.
31. Mura, C., and J. A. McCammon. 2008. Molecular dynamics of a kappaB DNA element: base flipping via cross-strand intercalative stacking in a microsecond-scale simulation. *Nucleic Acids Res.* 36:4941–4955.
32. Karatasos, K. 2013. Self-association and complexation of the anti-cancer drug doxorubicin with PEGylated hyperbranched polyesters in an aqueous environment. *J. Phys. Chem. B.* 117:2564–2575.
33. Gumbart, J., and K. Schulten. 2006. Molecular dynamics studies of the archaeal translocon. *Biophys. J.* 90:2356–2367.
34. Darden, T., D. York, and L. Pedersen. 1993. Particle mesh Ewald: an *N* log (*N*) method for Ewald sums in large systems. *J. Chem. Phys.* 98:10089–10092.
35. Feller, S. E., Y. H. Zhang, …, B. R. Brooks. 1995. Constant-pressure molecular dynamics simulation: the Langevin piston method. *J. Chem. Phys.* 103:4613–4621.
36. Olsson, M. H. M., C. R. Søndergaard, …, J. H. Jensen. 2011. PROPKA3: consistent treatment of internal and surface residues in empirical pKa predictions. *J. Chem. Theory Comput.* 7:525–537.
37. Humphrey, W., A. Dalke, and K. Schulten. 1996. VMD: visual molecular dynamics. *J. Mol. Graph.* 14:33–38.
38. Stone, J. 1998. An efficient library for parallel ray tracing and animation. M.S. thesis. University of Missouri-Rolla, Rolla, MO.
39. Schrödinger, L. L. C. 2010. The PyMOL Molecular Graphics System. http://www.pymol.org. Accessed January 21, 2014.
40. McClendon, C. L., L. Hua, …, M. P. Jacobson. 2012. Comparing conformational ensembles using the Kullback-Leibler divergence expansion. *J. Chem. Theory Comput.* 8:2115–2126.
41. Scarabelli, G., and B. J. Grant. 2014. Kinesin-5 allosteric inhibitors uncouple the dynamics of nucleotide, microtubule, and neck-linker binding sites. *Biophys. J.* 107:2204–2213.
42. Lange, O. F., and H. Grubmüller. 2006. Generalized correlation for biomolecular dynamics. *Proteins.* 62:1053–1061.
43. Michaud-Agrawal, N., E. J. Denning, …, O. Beckstein. 2011. MDAnalysis: a toolkit for the analysis of molecular dynamics simulations. *J. Comput. Chem.* 32:2319–2327.
44. Van Wart, A. T., J. Durrant, …, R. E. Amaro. 2014. Weighted implementation of suboptimal paths (WISP): an optimized algorithm and tool for dynamical network analysis. *J. Chem. Theory Comput.* 10:511–517.
45. Hagberg, A. A., D. A. Schult, and P. J. Swart. 2008. Exploring network structure, dynamics, and function using NetworkX. Gäel Varoquaux, Travis, Vaught, and Jarrod Millman, eds. P*roceedings of the 7th Python in Science Conference (SciPy2008)*, 11–15.
46. Brandes, U. 2001. A faster algorithm for betweenness centrality. *J. Math. Sociol.* 25:163–177.
47. Rice, J. A. 2007. Mathematical Statistics and Data Analysis, 3rd ed. Duxbury Press, Belmont, CA.
48. Roe, D. R., and T. E. Cheatham, 3rd. 2013. PTRAJ and CPPTRAJ: software for processing and analysis of molecular dynamics trajectory data. *J. Chem. Theory Comput.* 9:3084–3095.
49. Cuervo, A., P. D. Dans, …, L. Fumagalli. 2014. Direct measurement of the dielectric polarization properties of DNA. *Proc. Natl. Acad. Sci. USA.* 111:E3624–E3630.
50. Schutz, C. N., and A. Warshel. 2001. What are the dielectric "constants" of proteins and how to validate electrostatic models? *Proteins.* 44:400–417.

51. Miller, B. R., 3rd, T. D. McGee, Jr., …, A. E. Roitberg. 2012. MMPBSA.py: an efficient program for end-state free energy calculations. *J. Chem. Theory Comput.* 8:3314–3321.

52. Onufriev, A., D. Bashford, and D. A. Case. 2004. Exploring protein native states and large-scale conformational changes with a modified generalized born model. *Proteins.* 55:383–394.

53. Wood, C. M., J. M. Nicholson, …, J. P. Baldwin. 2005. High-resolution structure of the native histone octamer. *Acta Crystallogr. Sect. F Struct. Biol. Commun.* 61:541–545.

54. Shirts, M. R., and J. D. Chodera. 2008. Statistically optimal analysis of samples from multiple equilibrium states. *J. Chem. Phys.* 129:124105.

55. Biswas, M., J. Langowski, and T. C. Bishop. 2013. Atomistic simulations of nucleosomes. *WIREs Comput. Mol. Sci.* 3:378–392.

56. Biswas, M., K. Voltz, …, J. Langowski. 2011. Role of histone tails in structural stability of the nucleosome. *PLOS Comput. Biol.* 7: e1002279.

57. Khare, S. P., F. Habib, …, S. Galande. 2012. HIstome—a relational knowledgebase of human histone proteins and histone modifying enzymes. *Nucleic Acids Res.* 40:D337–D342.

58. Hornbeck, P. V., J. M. Kornhauser, …, M. Sullivan. 2012. PhosphoSitePlus: a comprehensive resource for investigating the structure and function of experimentally determined post-translational modifications in man and mouse. *Nucleic Acids Res.* 40:D261–D270.

59. Lange, O. F., and H. Grubmüller. 2008. Full correlation analysis of conformational protein dynamics. *Proteins.* 70:1294–1312.

60. Hoch, D. A., J. J. Stratton, and L. M. Gloss. 2007. Protein-protein Förster resonance energy transfer analysis of nucleosome core particles containing H2A and H2A.Z. *J. Mol. Biol.* 371:971–988.

61. Jin, C., and G. Felsenfeld. 2007. Nucleosome stability mediated by histone variants H3.3 and H2A.Z. *Genes Dev.* 21:1519–1529.

Supporting Materials: Effects of macroH2A and H2A.Z on nucleosome structure and dynamics as elucidated by molecular dynamics simulations

Samuel Bowerman and Jeff Wereszczynski*

Department of Physics and Center for Molecular Study of Condensed Soft Matter

Illinois Institute of Technology

Chicago, IL 60616, USA

*Corresponding author: jwereszc@iit.edu

1 Methods

1.1 System Construction and Simulation Details

The canonical nucleosome was initiated from the crystal structure of Davey *et al.* (PDB ID: 1KX5),[1] which includes the protruding N-terminal tails (except for the initial three residues of each H2B histone). The crystallographic Mn^{2+} were replaced by physiological Mg^{2+}. Additional Mg^{2+} ions were added to fill symmetrically suggested voids. The crystallographic waters were also maintained. The L1-Mutant structure was then created from the canonical one by mutating the ^{38}NYAE^{41} H2A L1 loops to ^{38}HPKY^{41} sequence of macroH2A. The mutation was done using VMD. The macroH2A system was initialized from the crystal structure solved by Chakravarthy *et al.* (PDB ID: 1U35).[2] The missing tail segments were constructed using the canonical structure as a reference. Strong similarities in DNA arrangement - particularly at DNA-protein binding sites (Figure S1) - allowed for the 146 base pairs of DNA from the crystal structure to be replaced by the 147 bp (plus Mg^{2+}) of the 1KX5 structure, and sequence divergent residues were mutated to match the sequence of the 1KX5 system. These actions were taken to ensure that differences between the systems were attributable only to H2A sequence divergence. The H2A.Z system was constructed analogously, using the crystal structure of Suto *et al.* (PDB ID: 1F66).[3] Therefore, each system was composed of 147 palindromic base pairs of α-satellite DNA wrapped around a histone core of *Xenopus laevis* H3, H4, and H2B with human H2A histones and variants. Histidine states were assigned using PROPKA and the interactive H-Bond Optimizer of the Desmond-Schrödinger package.[4]

Each system was simulated three times. Each simulation underwent 10,000 steps of geometric minimization (5,000 steps with protein heavy atoms harmonically restrained by a force constant of 10 kcal/mol/Å^2 and 5,000 steps without restraints). Heating was done by gradually raising the temperature from 10 to 300 K over 6 ps of simulation in the NVT ensemble. During heating, protein heavy atoms were harmonically restrained with a force constant of 10 kcal/mol/Å^2. The restraints were then gradually released over 600ps in the NPT ensemble.[5] Each simulation was then conducted for an additional 250ns in the NPT ensemble using a Langevin piston with a 100 fs period and collision frequency of 3 ps^{-1}. The SHAKE algorithm was used to allow for a 2 fs timestep, and long-range electrostatics were calculated using the particle mesh Ewald method.[6,7] Short range interactions were calculated with a 10 Å cutoff, where a switching function was applied at 8 Å. It was observed that ∼50ns was required for system equilibration (Figures S3-S6), and so ∼200ns of production data was obtained from each simulation (600ns per system) for analysis. For reference, one simulation could achieve a speed of ∼20ns per day on 256 processors on the XSEDE supercomputer Stampede, resulting in a cumulative cost of approximately 921,000 CPU hours.

Similarly, the 147bp of linear DNA was constructed in a 150mM NaCl box of TIP3P water, extending 10 Å from the solute. Following minimization and heating, three separate simulations were conducted in the NPT ensemble for an additional 60 ns. The initial 10ns of simulation were required for the RMSD to equilibrate, so only the last 50ns of each simulation was used during the MMGBSA analysis (150ns total). These simulations achieved similar speeds as the nucleosome simulations, requiring an additional 56,000 CPU hours (cumulative total of 976,296 hours).

1.2 Quantification of Equilibration Differences

To ensure that the modifications to the variant nucleosomes did not have a large effect on their equilibration dynamics, a separate trajectory was produced for the 1F66 H2A.Z nucleosome ("1F66 with tails"). In this system, the only modification to the crystal structure as the addition of histone tails. This structure was minimized and equilibrated analogously to the 250ns simulations, but the NPT simulation following heating was conducted for 50ns instead of the full 250ns. Equilibration times were determined by observing the backbone RMSD of the systems and by tail compaction (Figure S2A). Furthermore, the sampling differences between the 1F66 with tails simulation and the three 250ns simulations were compared against the inter-simulation differences of the 250ns set via the Kullback-Leibler Divergence of dihedral angle sampling. Local flexibility differences were compared via the "Mean Fluctuation Difference (MFD)." This metric measures the average difference of residue RMSF values of a target simulation (the "wild-type") against a reference set (the three 250ns simulations):

$$MFD = \frac{1}{N_s} \sum_{s=1}^{N_s} \left(\sum_{i=1}^{N_{residues}} [RMSF(i)_{wild-type} - RMSF(i)_s] \right) \quad (1)$$

where N_s is equal to 3, for the three 250ns simulations. In order to create a consistent sampling space for all comparison measurements, the three 250ns H2A.Z simulations were concatenated to include only the first 50ns.

1.3 MM/GBSA Analysis

It is important to note that the MM/GBSA approach is typically done in one of two ways: the single trajectory and the three-trajectory methods. In the single trajectory approach, the complex is separated into receptor and ligand components using coordinates produced in the complex assembly simulation. In the three-trajectory approach, the coordinates for analysis are taken from three separately simulated states (complex, receptor only, and ligand only). The three-trajectory approach supposes that the ligand and receptor components exist in substantially different conformations when separated from one another. For the nucleosome, this is clearly true for supercoiled DNA,[8] but is unclear for the histone core. However, the crystal structure of the octamer, *sans* DNA, still shows the colloquial histone fold, albeit under 2M salt concentration.[9] Furthermore, the free energy of construction for the octamer ($\Delta G_{octamer}$) — calculated using an MM/GBSA analysis on the extracted coordinates — was approximately -200 kcal/mol across all four systems, suggesting that the octamer core is stable on the hundreds of nanoseconds timescales that we are capable of observing. It is also worth noting that simulation costs are strongly affected by the number of atoms, which is primarily dictated by the size of the octamer in nucleosome simulations. Thus, separate simulations of each octamer system would effectively double the simulation cost with little payoff in the accessible timescales. Therefore, a hybrid, two-trajectory approach was taken in which protein coordinates were extracted from the nucleosome assembly for each separate system while simulating a separate set of coordinates for the DNA (which could be applied against all four systems).

1.4 Allosteric Calculations

Residue correlations were calculated using the "largest linear mutual information" method.[10,11] In this method, the linear mutual information is calculated between all heavy atoms in the system. The residue-wise mutual information values were converted to a Pearson correlation coefficient-like value by $r_{i,j} = [1 - e^{(-2I_{i,j}/3)}]^{1/2}$, where $I_{i,j}$ is the largest linear mutual information between any two atoms of the residues i and j.

Contact maps were produced in-house using the MDAnalysis package.[12] Two residues were considered to be in contact if their C_α (protein) or C1' (nucleic) atoms were within 10 Å for 70% of the configurations. Using the predefined correlation matrices and this contact map, a NetworkX edgelist was formed.[13] The length of each edge was defined by $D_{i,j} = -log(r_{i,j})$, where $r_{i,j}$ is the correlation value between residues i and j. The optimal paths were calculated using the NetworkX implementation of Dijkstra's algorithm, and the sub-optimal paths were determined using Yen's K-Shortest Paths algorithm.

The Kullback-Leibler Divergence of dihedral angles were calculated using the method of McClendon.[14] In this method, each simulation was separated into three blocks (9 blocks per system) with 31,666 configurations (roughly 63.3 ns) per block. Histogram widths were 15 degrees. The Kullback-Leibler Divergence values were calculated for each variant by using the populations of the canonical system as a reference set. Bootstrapping techniques were employed to calculate the self-divergence of the canonical system. For any residue in a variant system whose divergence value was below this self-divergence threshold, the KL-Divergence value for that residue was set to 0.

1.5 Edge-betweenness Centrality

The importance of a node in a communication network can be defined by its edge-betweenness centrality.[15] In this method, the "shortest" correlation pathway between all residue-pairs is calculated. A residue's edge-betweenness centrality is then defined as the number of shortest paths in which the residue appears:

$$C(i) = \frac{1}{N} \sum_{s \neq t \neq i} x_i\,(s,t) \tag{2}$$

where N is the total number of paths and $x_i(s,t)$ is either 0 (residue i does not exist in path between residues s and t) or 1 (residue i does exist in said path). For visualization purposes, centrality values are normalized such that the minimum centrality is 0 and the maximum centrality is 1, according to the formula:

$$C_{norm}\,(i) = \frac{C(i) - C_{min}}{C_{max} - C_{min}} \tag{3}$$

where C_{max} and C_{min} are the maximum and minimum centrality values in the network.

From the plot of normalized centrality value vs percentile (Figure S11), we observe that the difference in centrality between percentile increments is not constant but is large at the upper and lower quartiles and steady in the interquartile region. The inflection point of the upper quartile exists near the tenth percentile, so we have chosen this location as our cut-off

for defining allosteric "hotspots."

We were able to identify several well-known post-translational modifications (PTMs) in the canonical nucleosome by our betweenness centrality measurement.[16–18] In the canonical system, we observe 6 of 23 mononucleosome altering PTM sites (monoNCP PTMs) in the upper tenth percentile and 12 of 23 in the upper quartile. The significance of observing this subset of residues in each percentile was tested by calculating the pmf of a hypergeometric distribution,[19]

$$\mathrm{pmf}\,(x = k) = \frac{\binom{K}{k}\binom{N-K}{n-k}}{\binom{N}{n}} \tag{4}$$

where N is the total number of protein residues (487), n is the percentile population size (n=49 for the upper tenth, and n=122 for the upper quartile), K is the total number of monoNCP PTM residues (23), and k is the number of observed monoNCP PTM sites (k=6 for the upper tenth, and k=12 for the upper quartile). Using these values, the upper tenth percentile observation has a p-value of 0.0155, and the upper quartile p-value is 0.00288. Therefore, the observation that monoNCP PTMs are located at allosteric hotspots is statistically significant.

Furthermore, we can quantify the presence of monoNCP PTMs at allosteric hotspots by calculating the enrichment factor (EF) of monoNCP PTMs over random selection,

$$EF = \frac{k}{K}\frac{N}{n} \tag{5}$$

where the variables have the same meaning as for the hypergeometric distribution. We then calculate an EF of 2.54 for monoNCP PTM presence at allosteric hotspots. A plot of EF vs centrality percentile can be found in Figure S13.

2 Equilibration Comparison

The equilibration time for the 1F66 with tails simulation was measured via backbone RMSD values and histone tail compaction, and it was found to be in agreement with the three production H2A.Z simulations (Figure S2A-B). Furthermore, the MFD values obtained by comparing the 1F66 with tails simulation against the set of three production simulations show that local fluctuation differences are comparable to the inter-simulation average for the production set (Figure S2C). In this metric, the fluctuations in the histone core and DNA are less than 1 Å, on average, while the histone tails exhibit a wider deviation in fluctuations. These values are consistent with the noise present in comparing the fluctuations between the set of H2A.Z production simulations. Lastly, individual residue sampling was compared using the Kullback-Leibler Divergence of dihedral angle sampling. From these calculations, the average divergence value between the 1F66 with tails simulation and the three 250ns simulations was 0.596 (σ=1.06). The residue-averaged Kullback-Leibler divergence value for comparisons between each of the 250ns was 0.531 (σ=1.03), showing that the differences in local sampling of the 1F66 with tails simulation and the three 250ns simulations was comparable to the noise between simulations of identical systems.

References

[1] Davey,C.A., Sargent,D.F.; Luger,K., Maeder,A.W. and Richmond,T.J. Solvent Mediated Interactions in the Structure of the Nucleosome Core Particle at 1.9Å Resolution. *J. Mol. Biol.* **2002**, *319*, 1097 – 1113.

[2] Chakravarthy,S., Gundimella,S.K., Caron,C., Perche,P.Y., Pehrson,J.R., Khochbin,S. and Luger,K. Structural characterization of the histone variant macroH2A. *Mol. Cell. Biol.* **2005**, *25*, 7616–7624.

[3] Suto,R.K., Clarkson,M.J., Tremethick,D.J. and Luger,K. Crystal structure of a nucleosome core particle containing the variant histone H2A.Z. *Nat. Struct. Biol.* **2000**, *7*, 1121–1124.

[4] Olsson,M. H.M., Søndergaard,C.R., Rostkowski,M. and Jensen,J.H. PROPKA3: Consistent Treatment of Internal and Surface Residues in Empirical pKa Predictions. *J. Chem. Theor. Comp.* **2011**, *7*, 525–537.

[5] Feller,S.E., Zhang,Y.H., Pastor,R.W. and Brooks,B.R. Constant-pressure molecular-dynamics simulation - the langevin piston method. *J. Chem. Phys.* **1995**, *103*, 4613–4621.

[6] Ryckaert,J.P., Ciccotti,G. and Berendsen,H.J. Numerical integration of the cartesian equations of motion of a system with constraints: molecular dynamics of n-alkanes. *J. Comp. Phys.* **1977**, *23*, 327 – 341.

[7] Darden,T., York,D. and Pedersen,L. Particle mesh Ewald: An N log (N) method for Ewald sums in large systems. *J. Chem. Phys.* **1993**, *98*, 10089–10092.

[8] Bishop, T.C. Molecular dynamics simulations of a nucleosome and free DNA. *J. Biomol. Struct. Dyn.* **2005**, *22*, 673–686.

[9] Wood,C.M., Nicholson, J.M., Lambert, S.J., Chantalat, L., Reynolds, C.D., and Baldwin,J.P. High-resolution structure of the native histone octamer. *Acta Crystallogr. F* **2005**, *61*, 541–545.

[10] Lange,O.F. and Grubmuller,H. Generalized correlation for biomolecular dynamics. *Proteins* **2006**, *62*, 1053–1061.

[11] Scarabelli,G. and Grant,B.J. Kinesin-5 allosteric inhibitors uncouple the dynamics of nucleotide, microtubule, and neck-linker binding sites. *Biophys. J.* **2014**, *107*, 2204–2213.

[12] Michaud-Agrawal,N., Denning,E., Woolf,T. and Beckstein,O. MDAnalysis: A Toolkit for the Analysis of Molecular Dynamics Simulations. *J. Comp. Chem.* **2011**, *32*, 2319–2327.

[13] Hagberg,A.A., Schult,D.A. and Swart,P.J. Exploring network structure, dynamics, and function using NetworkX. Proceedings of the 7th Python in Science Conference (SciPy2008). Pasadena, CA USA, 2008, pp 11–15.

[14] McClendon,C.L., Hua,L., Barreiro,A. and Jacobson,M.P. Comparing Conformational Ensembles Using the Kullback-Leibler Divergence Expansion. *J. Chem. Theor. Comp.* **2012**, *8*, 2115–2126.

[15] Brandes,U. A faster algorithm for betweenness centrality. *J. Math. Sociol.* **2001**, *25*, 163–177.

[16] Bowman,G.D. and Poirier,M.G. Post-translational modifications of histones that influence nucleosome dynamics. *Chem. Rev.* **2015**, *115*, 2274–2295.

[17] Khare,S.P., Habib,F., Sharma,R., Gadewal,N., Gupta,S., and Galande,S. HIstome–a relational knowledgebase of human histone proteins and histone modifying enzymes. *Nucl. Acids Res.* **2012**, *40*, D337–342.

[18] Hornbeck,P.V., Kornhauser,J.M., Tkachev,S., Zhang,B., Skrzypek,E., Murray,B., Latham,V. and Sullivan,M. PhosphoSitePlus: a comprehensive resource for investigating the structure and function of experimentally determined post-translational modifications in man and mouse. *Nucl. Acids Res.* **2012**, *40*, D261–270.

[19] Rice,J.A. *Mathematical Statistics and Data Analysis*, 3rd ed., Duxbury Press: Belmont, CA, 2007.

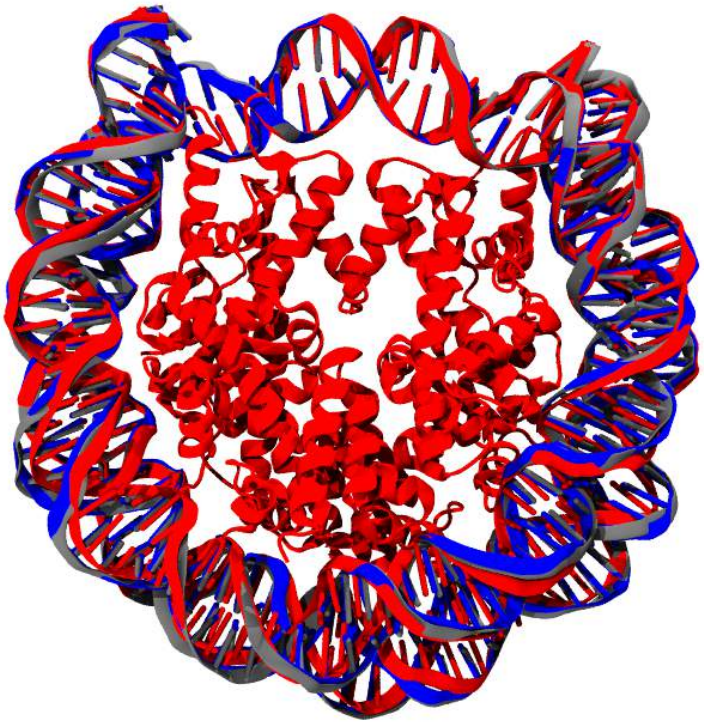

Figure S1: Comparison of crystallographic DNA arrangment in the canonical (blue), macroH2A (red), and H2A.Z (grey) nucleosomes. As expected, the DNA-histone binding sites show strong agreement in coordination between the three structures.

System	H2A R^{29}-DNA	H2B S^{33}-DNA	L1-L1	Dimer-tetramer
Canonical NCP	63%	40%	0.5 ± 0.1	14.8 ± 1.1
L1 Mutant	70%	60%	0.4 ± 0.1	16.5 ± 1.0
macroH2A NCP	52%	30%	0.2 ± 0.1	14.7 ± 0.8
H2A.Z NCP	73%	85%	0.1 ± 0.1	14.4 ± 1.1

Table S1: Hydrogen bonding at key locations in the nucleosome. For the H-Bonds formed with the DNA, the occupancy of each bond is given. For the other interactions, the average number of hydrogen bonds between each group in a given frame is listed.

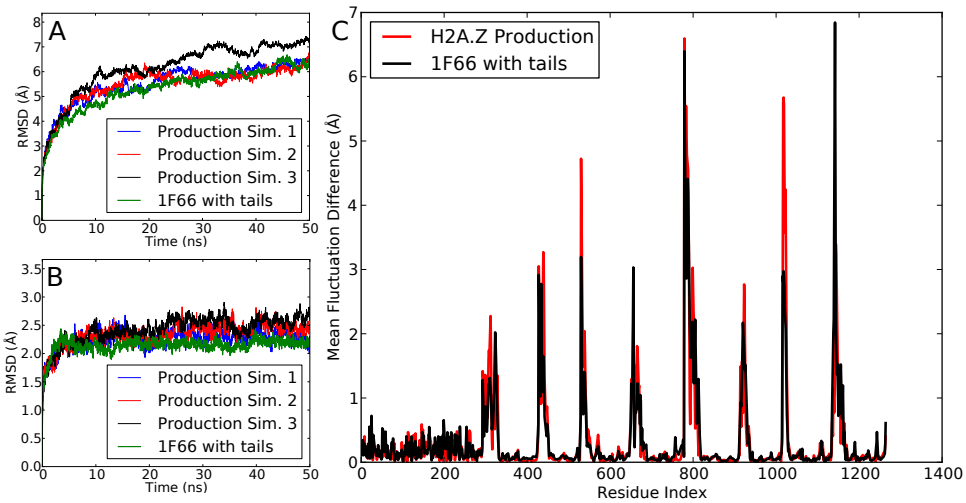

Figure S2: Backbone RMSD timeseries for (A) the whole system and (B) the nucleosome core, including DNA. Displayed are the three production simulations of H2A.Z (blue,red,black), as well as the 50ns 1F66 with tails simulation (green). The 1F66 with tails simulation shows no change in required equilibration time. (C) per-Residue Mean Fluctuation Difference (MFD) plotted for the 1F66 with tails simulation referenced against the set of three production simulations (black). With the exception of the histone tails, the MFD of the 1F66 with tails simulation differs less than 1 Å from the production runs of H2A.Z. This is comparable to the noise present when comparing the three different production simulations of H2A.Z (red).

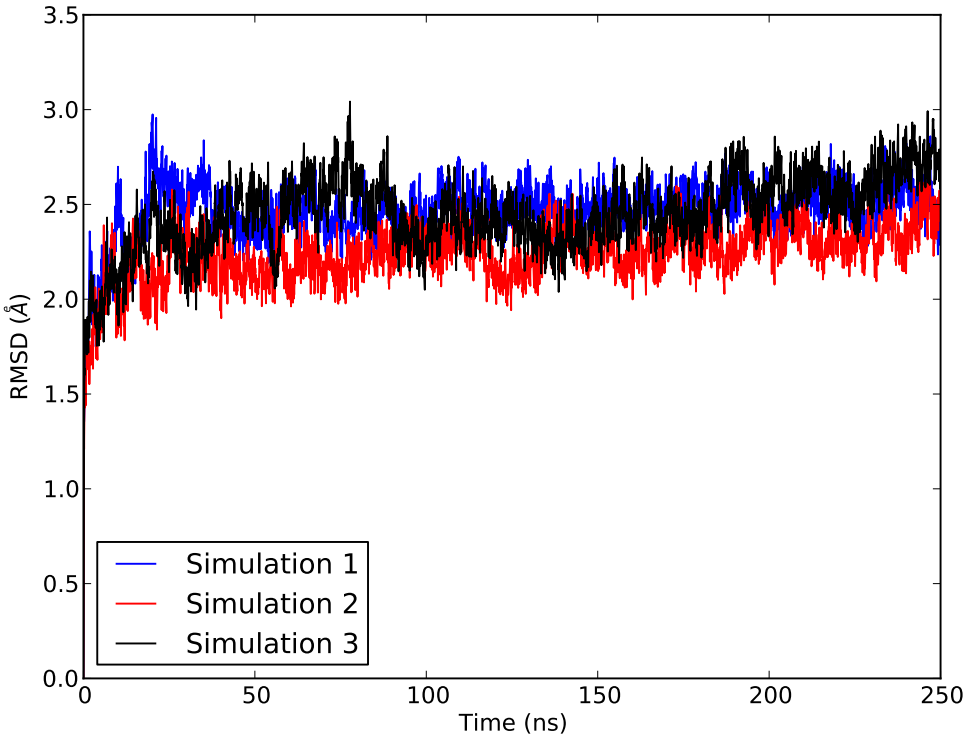

Figure S3: Backbone RMSD of three canonical simulations. The simulations were fit to the histone core backbone, and the RMSD calculations were done on the DNA and histone core backbone atoms, excluding tail residues.

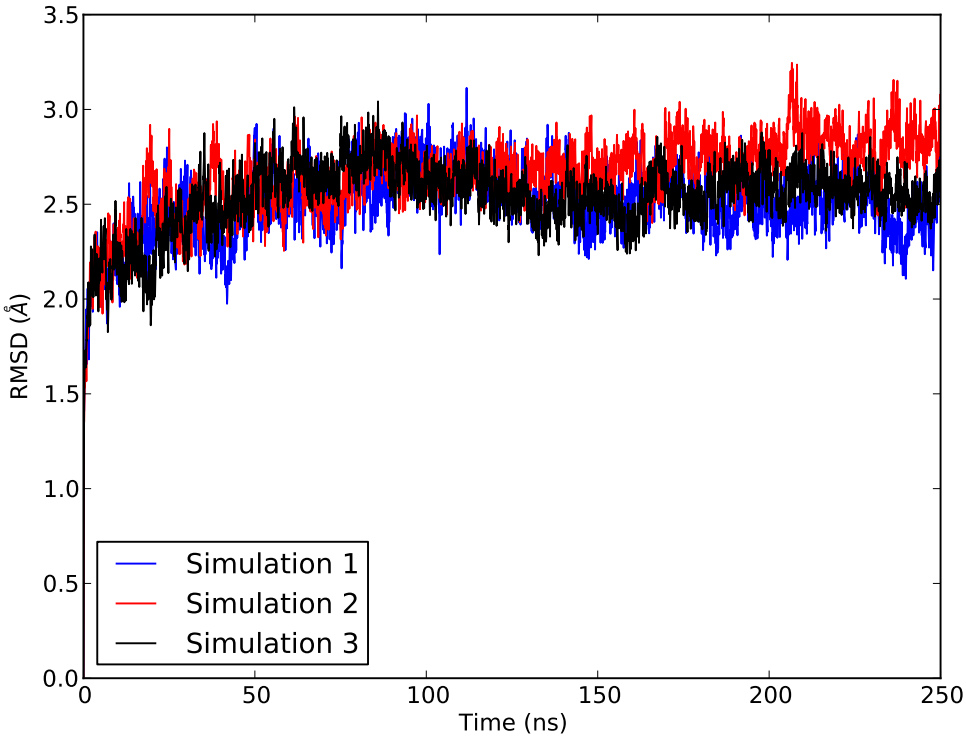

Figure S4: Backbone RMSD of three L1-Mutant simulations. The simulations were fit to the histone core backbone, and the RMSD calculations were done on the DNA and histone core backbone atoms, excluding tail residues.

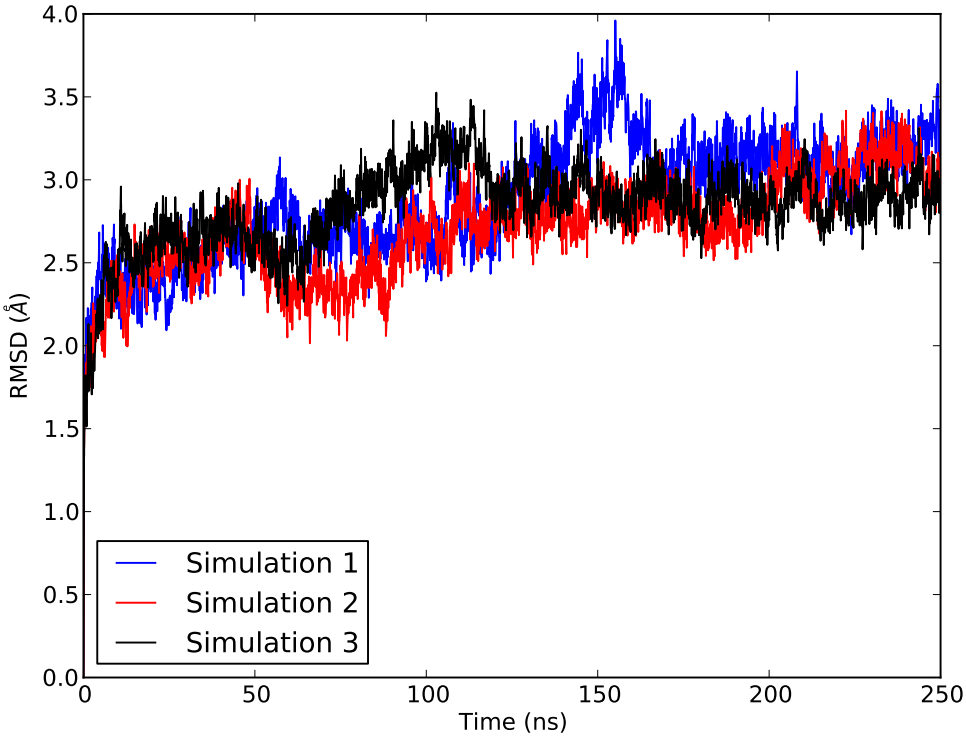

Figure S5: Backbone RMSD of three macroH2A simulations. The simulations were fit to the histone core backbone, and the RMSD calculations were done on the DNA and histone core backbone atoms, excluding tail residues.

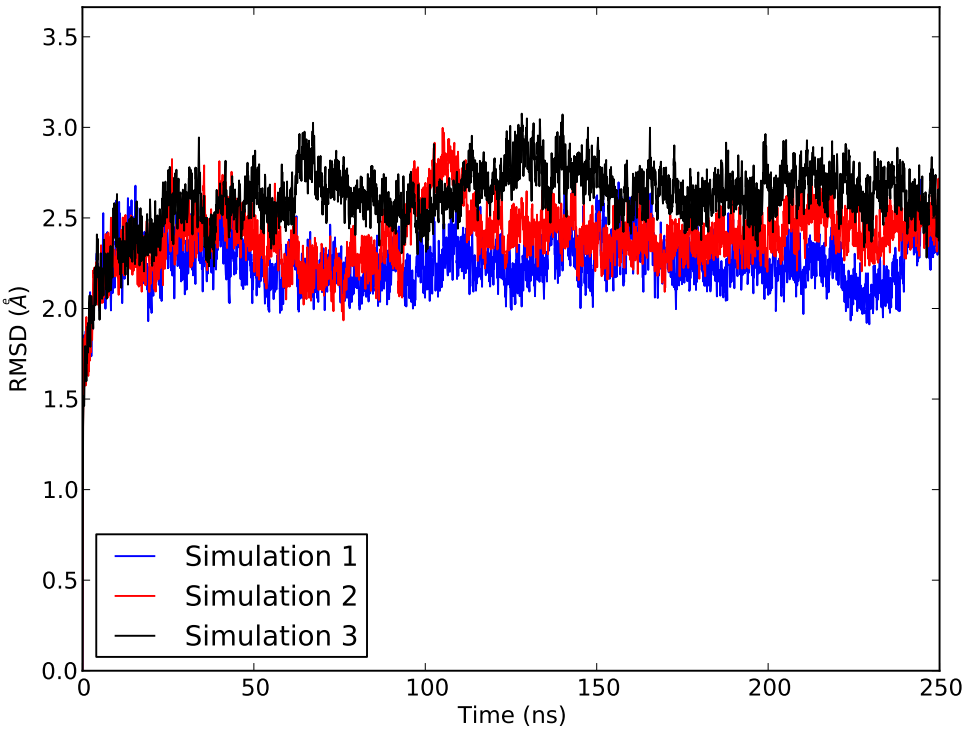

Figure S6: Backbone RMSD of three H2A.Z simulations. The simulations were fit to the histone core backbone, and the RMSD calculations were done on the DNA and histone core backbone atoms, excluding tail residues.

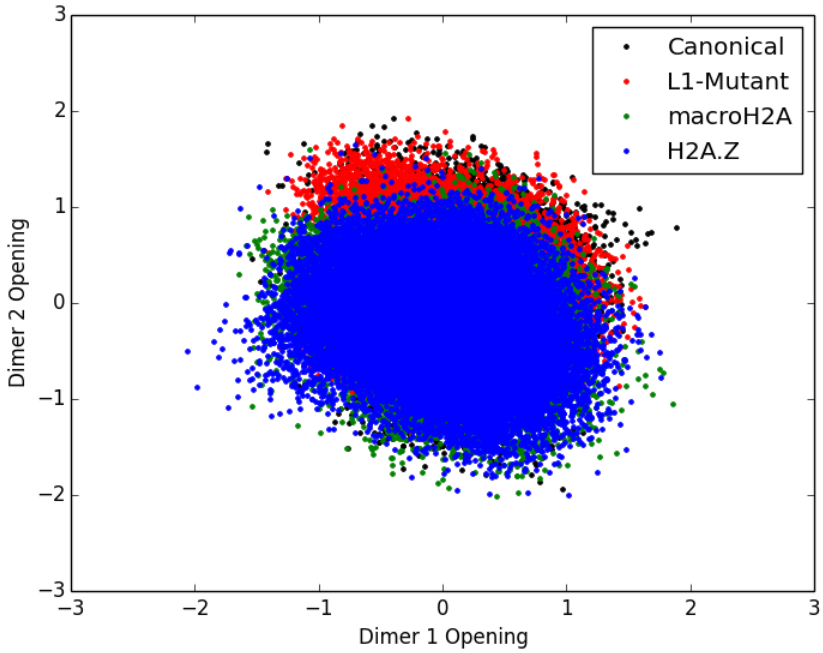

Figure S7: Dimer dissociation phase space for the nucleosome systems. All systems sample the same region of this space, which suggests that H2A composition has little effect on dimer dissociation in the hundreds of nanoseconds timescale. For reference, the dimer separation event occurs on the millisecond timescale.

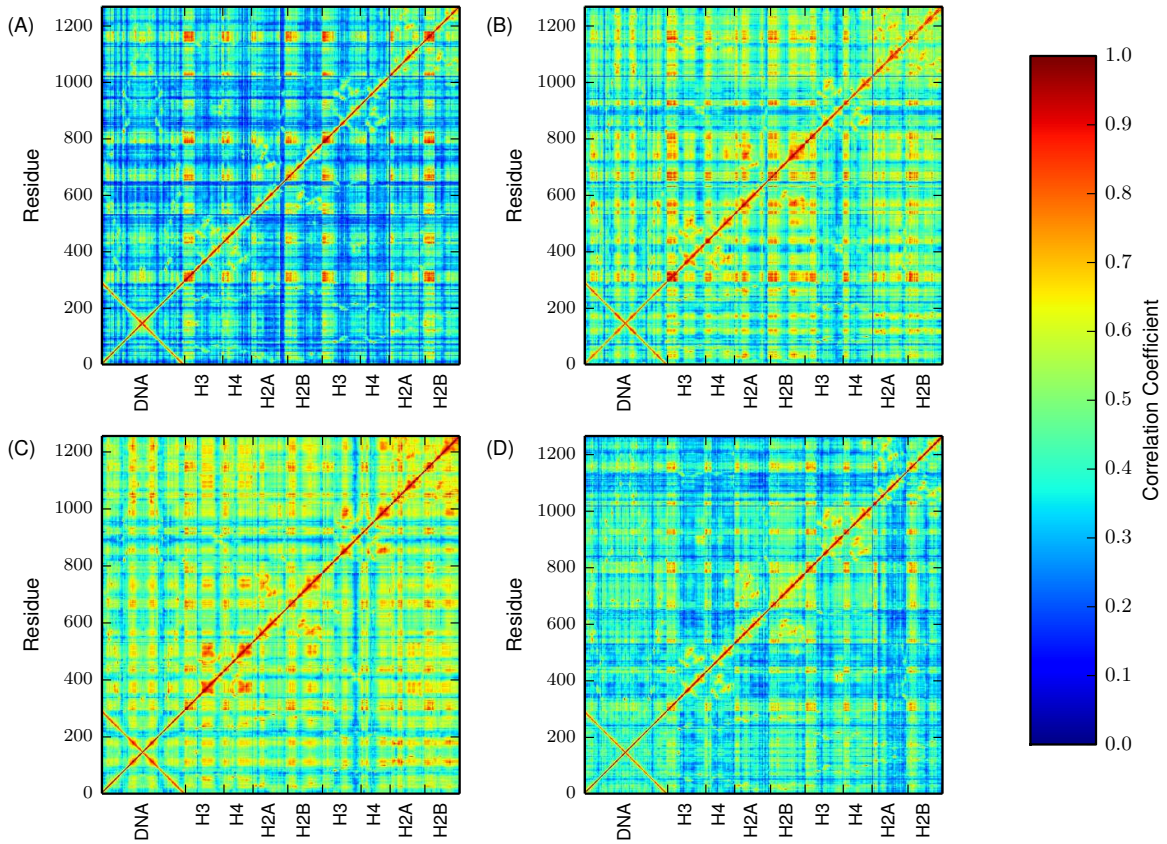

Figure S8: Pearsified Largest Linear Mutual Information matrices for (a) canonical, (b) L1-Mutant, (c) macroH2A, and (d) H2A.Z nucleosomes. The canonical NCP shows the weakest average correlation across the whole molecule, and the macroH2A variant shows the strongest. The L1-Mutant correlation strengths are similar to macroH2A, while the H2A.Z nucleosome shows correlations that are slightly above the levels of the canonical nucleosome. The steady increase in correlations within the variant systems is likely a result of favorable changes in interhistone interactions.

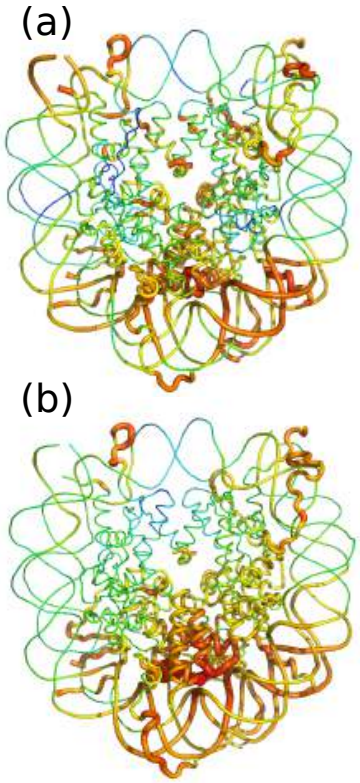

Figure S9: Average individual residue correlation with L1 loop residues for (a) canonical and (b) L1-Mutant nucleosomes. Thicker, redder residues are those with stronger average correlations with the L1 loop sequence. The L1-Mutant nucleosome shows increased correlations near the L1-L1 interface, as well as among H2B-H4 four helix bundle residues. Both systems display appreciable correlations between the L1 loops and docking domain residues in the dimer and tetramer. Histone tails were truncated to improve clarity.

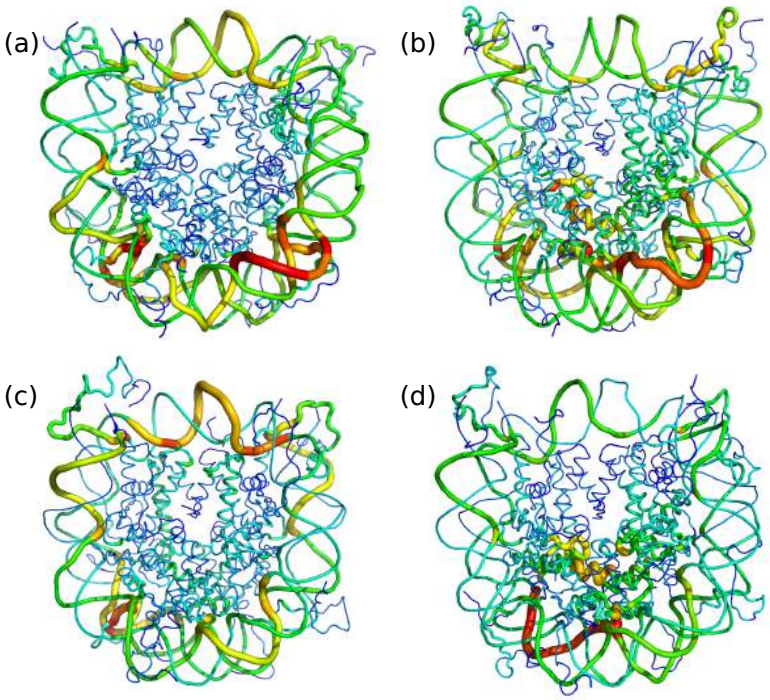

Figure S10: Edge-betweenness centrality for (a) canonical, (b) L1-Mutant, (c) H2A.Z, and (d) macroH2A nucleosomes. Brighter, wider regions represent locations that are accessed more frequently in the optimal communication pathways of each nucleosome system. The H2A L1-L1 interaction region in the L1-Mutant and macroH2A systems act as communication hubs for allosteric networks in the nucleosome, whereas the canonical and H2A.Z nucleosomes rely heavier on DNA to propagate information.

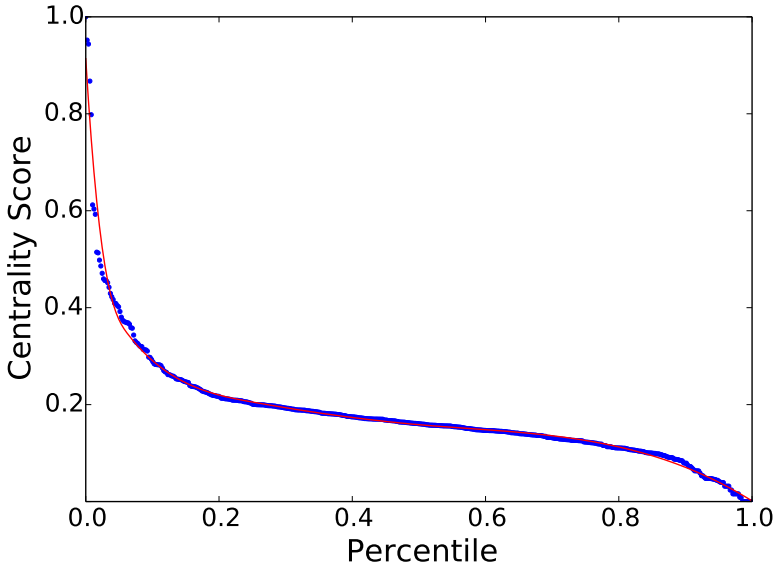

Figure S11: Centrality scores vs percentile ranking (blue dots) for the canonical nucleosome. The spline fit is represented in red. The drastic change in centrality score in the upper quartile indicates that residues rely heavily on several key residues for information propagation. The inflection point of this trend is located at the tenth percentile.

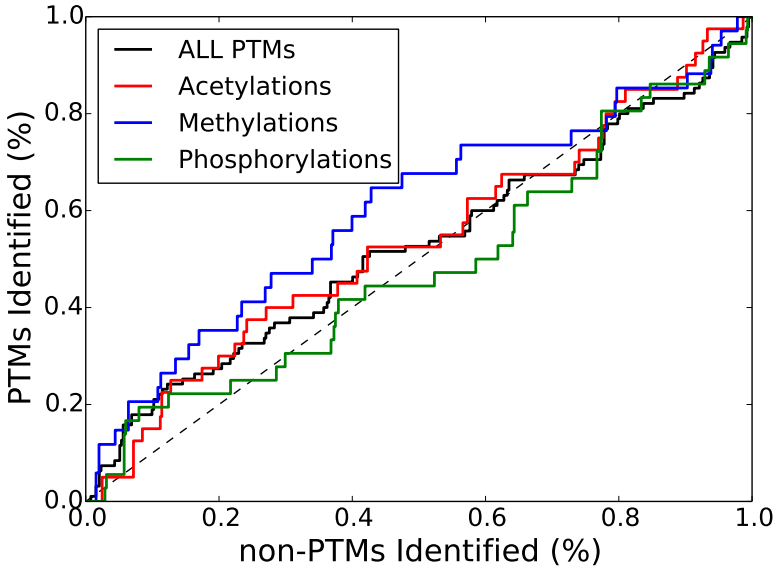

Figure S12: ROC plot for the canonical nucleosome with PTMs separated by modification type. Methylations exist most prevalently as allosteric hotspots, and acetylations are the least prevalent. The early enrichment of methylations is a result of their presence near DNA extremities and between superhelical DNA turns where pathways cross the symmetries.

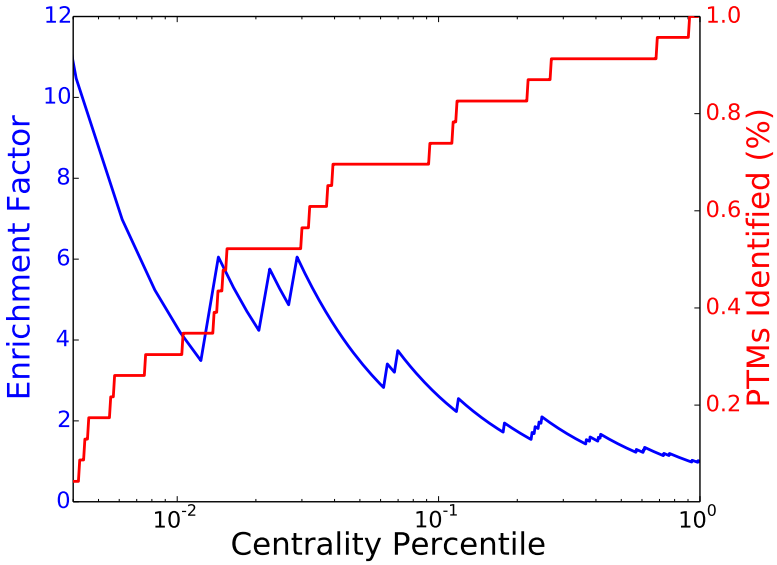

Figure S13: Enrichment Factor (blue) and monoNCP PTM identification percent (red) as functions of centrality percentile in the canonical nucleosome. We observe a strong degree of early enrichment for identifying monoNCP PTMs at allosteric hotspots. At the cutoff of the tenth percentile, we observe an EF of 2.54.

Table S2: Protein-normalized centrality values for the 23 monoNCP PTM targets. The percentile rank of each value is also listed. The residues in the upper quartile are listed in bold. Those in the upper tenth percentile are italicized. PTM sites that have significantly smaller centrality values than neighboring sequence residues in the upper quartile are labeled by an (*) and the value of the neighbor is reported.

	Canonical		L1-Mutant		macroH2A		H2A.Z	
PTM	Centrality	Percentile	Centrality	Percentile	Centrality	Percentile	Centrality	Percentile
H3 K4me3	0.05	6.6	0.07	6.3	0.05	6.2	0.06	6.7
H3 K9ac	0.13	27.0	0.19	22.6	0.14	24.8	0.16	27.5
H3 K14ac	0.20	**75.6**	0.30	51.0	0.23	53.4	0.26	61.2
H3 K18ac	0.27	**87.9**	0.39	73.9	0.30	69.8	0.34	**78.4**
H3 K23ac	0.34	***92.8***	0.51	**87.3**	0.38	**82.0**	0.44	**88.9**
H3 K36me2,3	0.47	***97.5***	0.80	***97.3***	0.45	**86.1**	0.69	***97.7***
H3 Y41ph	0.46	***96.9***	1.00	***100.0***	0.67	***96.9***	0.84	***99.8***
H3 R42me2a	0.51	***98.4***	0.79	***96.7***	0.37	**81.5**	0.79	***99.2***
H3 T45ph*	0.29	**75.0**	0.38	71.1	0.22	52.4	0.28	67.0
H3 K56ac	0.17	58.9	0.18	20.1	0.22	52.4	0.19	35.6
H3 S57ph	0.15	39.0	0.16	17.9	0.22	52.4	0.16	28.6
H3 K64ac	0.15	42.7	0.26	38.0	0.27	63.6	0.21	46.1
H3 K115ac	0.15	38.4	0.13	11.7	0.06	8.5	0.24	53.9
H3 T118ph	0.37	***93.4***	0.43	**81.9**	0.14	25.8	0.63	***96.5***
H3 K122ac	0.23	**81.9**	0.29	47.4	0.13	23.9	0.39	**82.7**
H4 K16ac	0.21	**77.0**	0.38	70.0	0.16	33.9	0.18	34.2
H4 S47ph*	0.25	**85.4**	0.28	43.9	0.19	44.3	0.34	**78.2**
H4 K77ac	0.18	61.8	0.29	45.2	0.15	28.3	0.25	58.0
H4 K79ac*	0.31	***91.4***	0.34	63.8	0.56	***95.0***	0.35	**79.8**
H4 K91ac	0.12	23.4	0.38	70.0	0.57	***95.4***	0.29	68.9
H4 R92me	0.21	**76.4**	0.53	**88.5**	0.81	***99.4***	0.33	**77.6**
H2B K30ar	0.94	***99.6***	0.81	***97.7***	0.26	62.4	0.72	***98.8***
H2B K123ub1	0.00	0.0	0.00	0.0	0.00	0.0	0.00	0.0

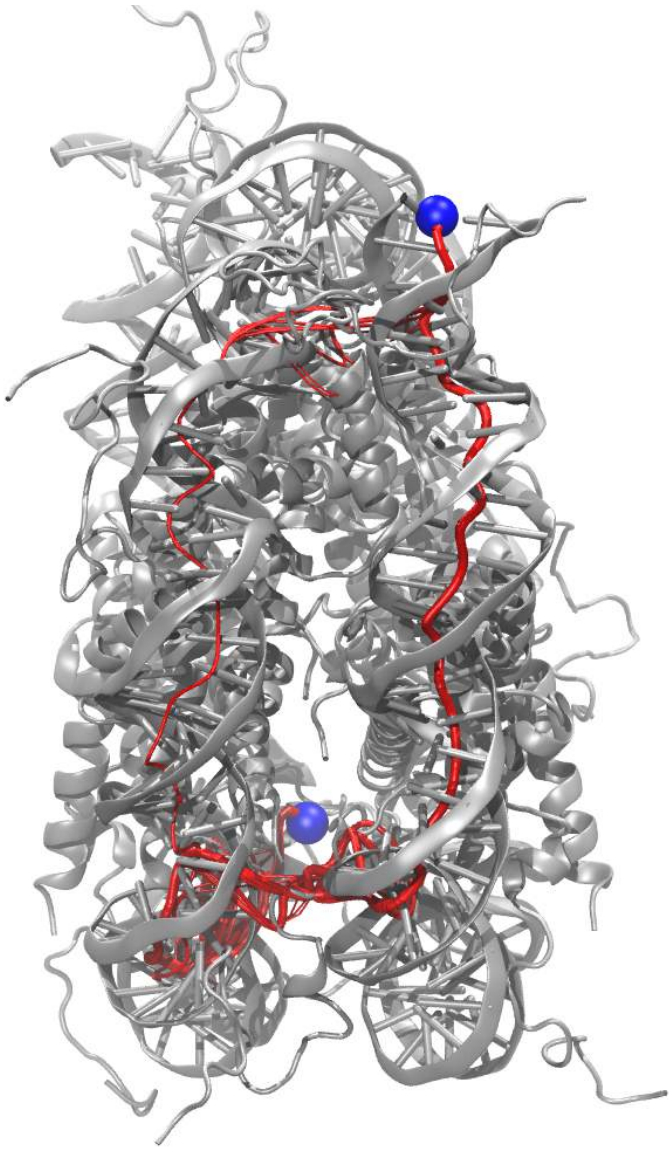

Figure S14: Sub-optimal pathways for L1 loop to DNA exit in the canonical nucleosome.

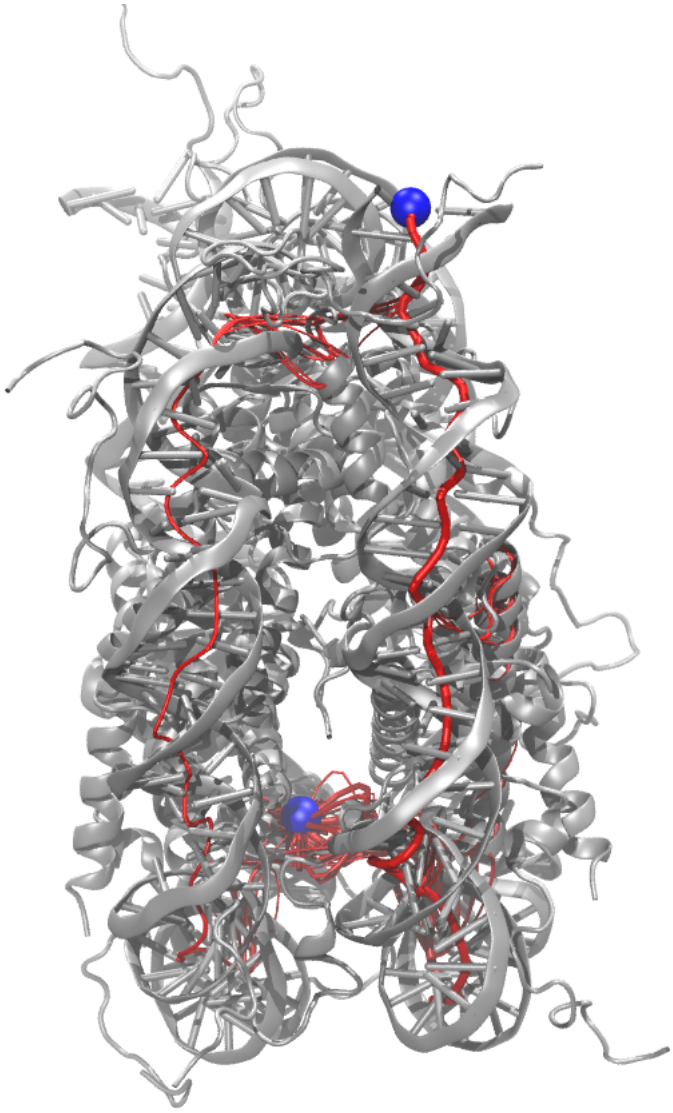

Figure S15: Sub-optimal pathways for L1 loop to DNA exit in the L1-Mutant nucleosome.

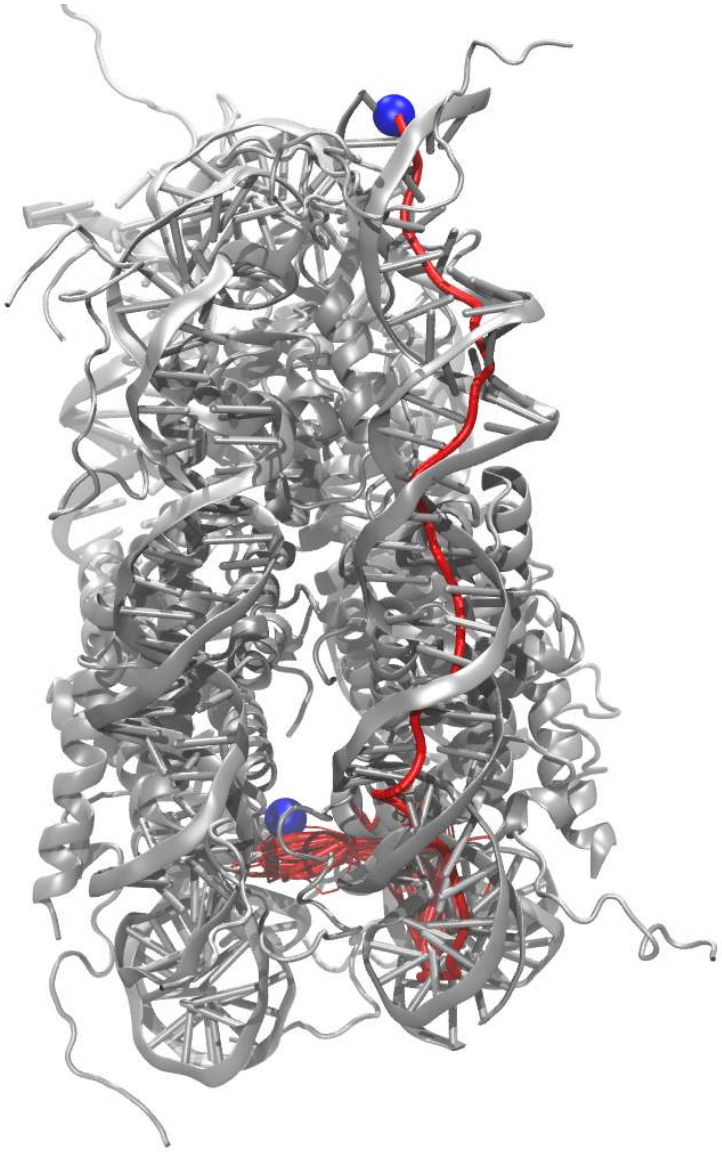

Figure S16: Sub-optimal pathways for L1 loop to DNA exit in the macroH2A nucleosome.

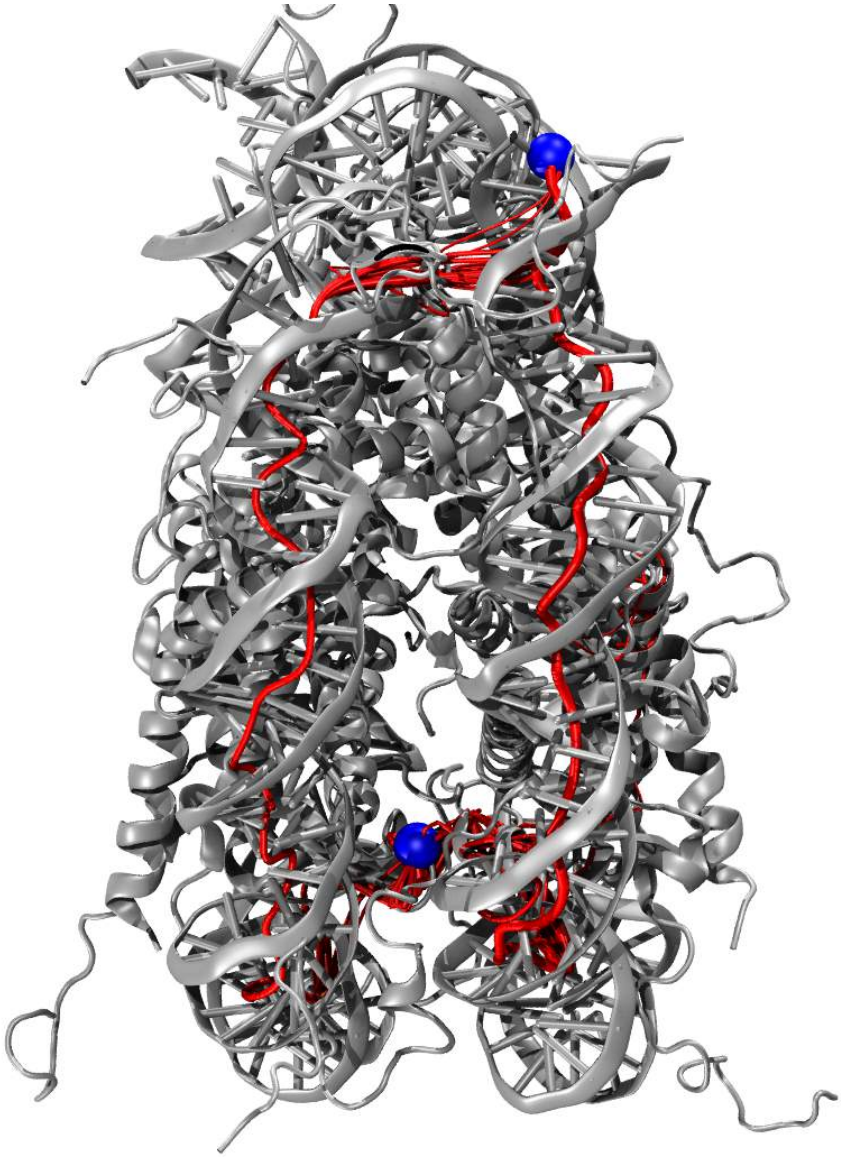

Figure S17: Sub-optimal pathways for L1 loop to DNA exit in the H2A.Z nucleosome.

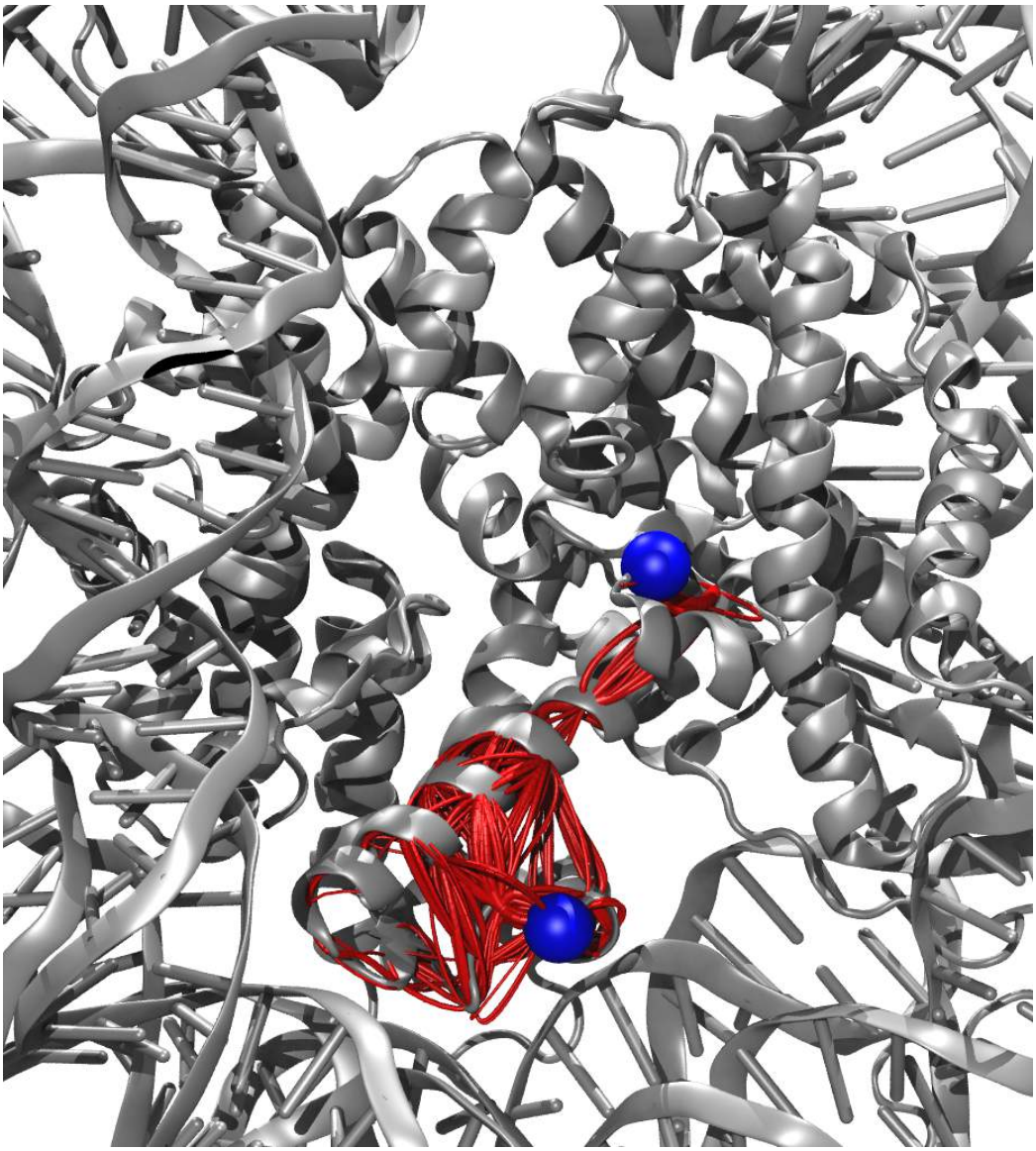

Figure S18: Sub-optimal pathways for L1 loop to the associated docking domain in the canonical nucleosome. The opposing dimer has been removed to improve visualization clarity.

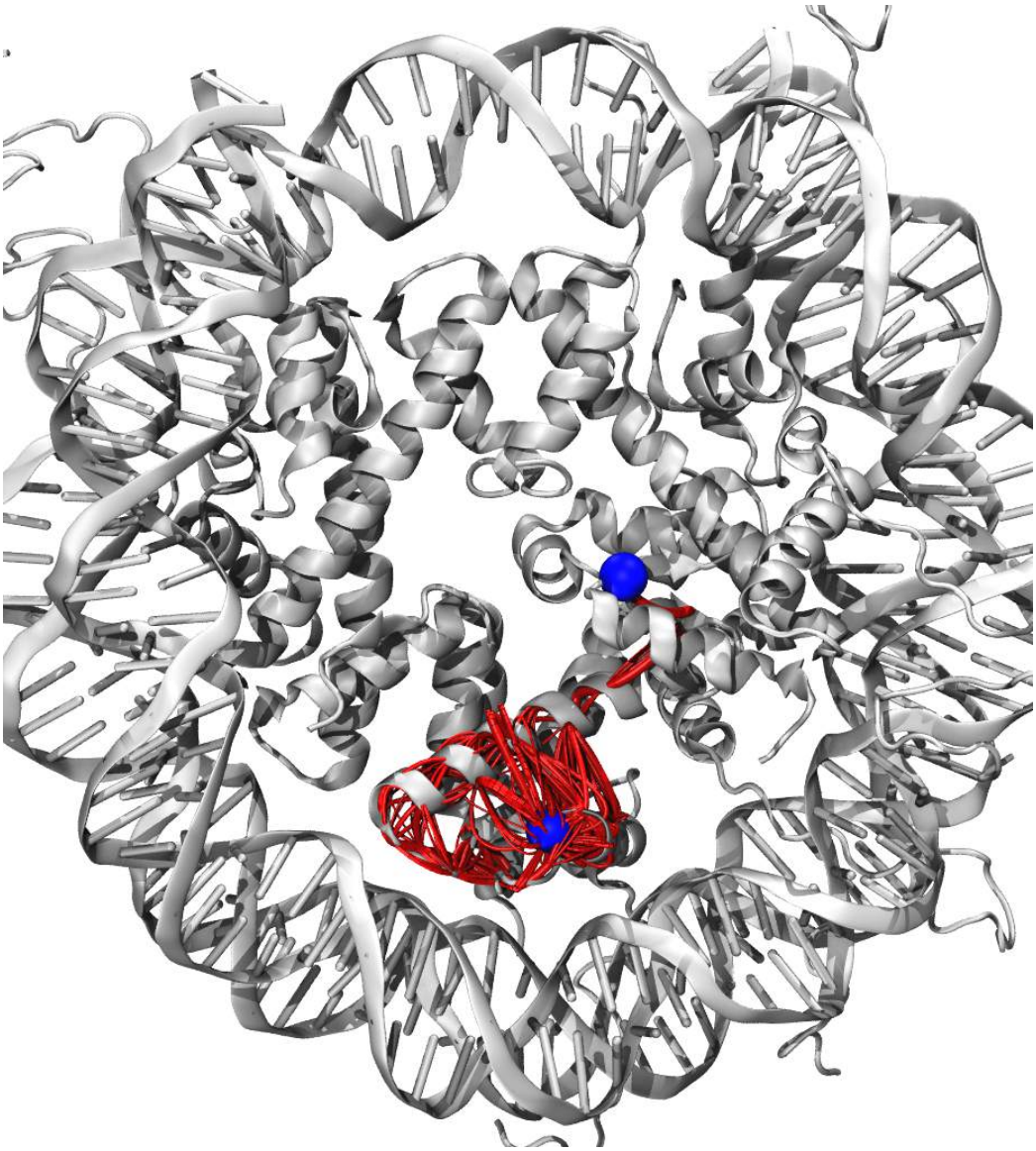

Figure S19: Sub-optimal pathways for L1 loop to the associated docking domain in the L1-Mutant nucleosome. The opposing dimer has been removed to improve visualization clarity.

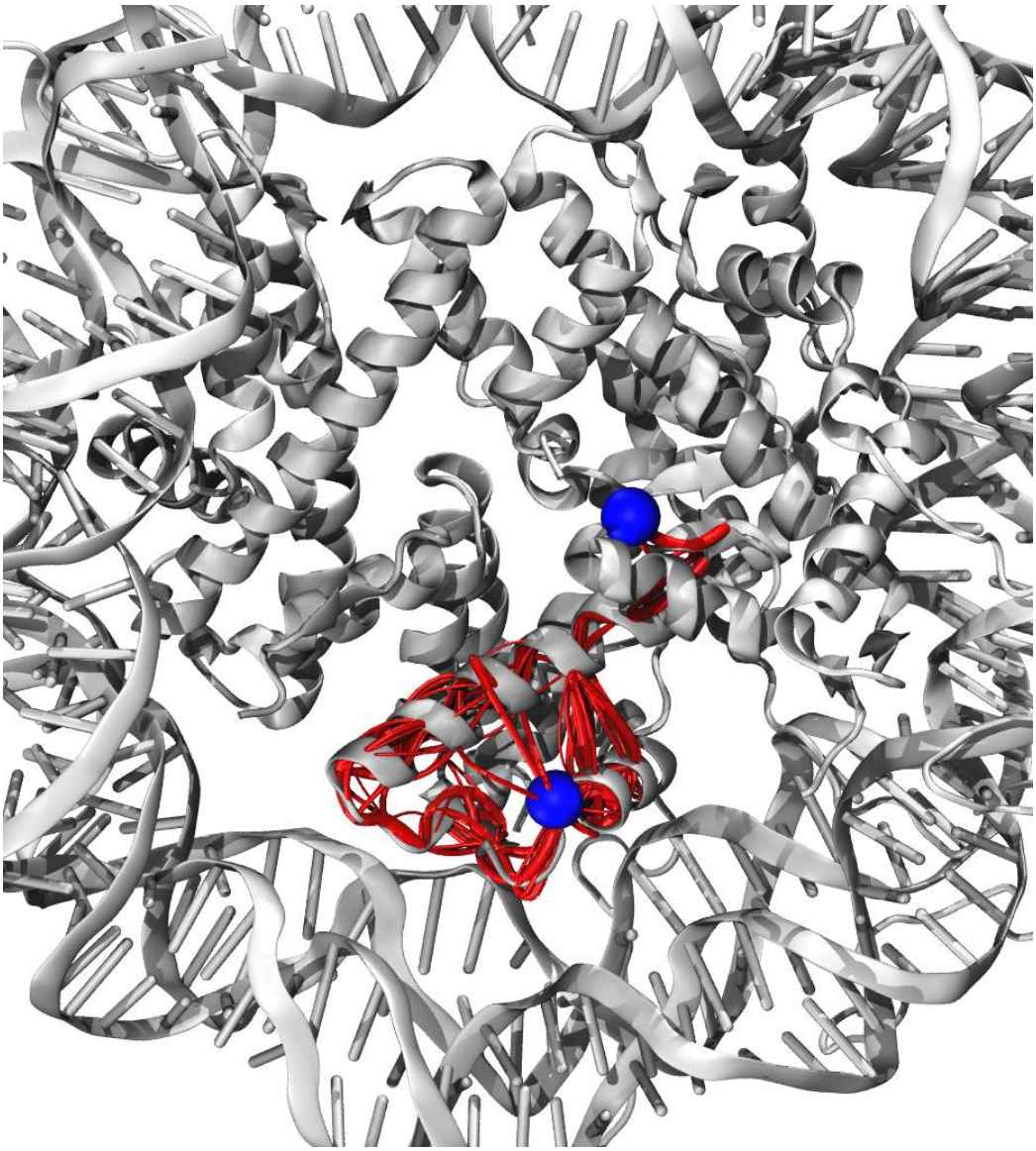

Figure S20: Sub-optimal pathways for L1 loop to the associated docking domain in the macroH2A nucleosome. The opposing dimer has been removed to improve visualization clarity

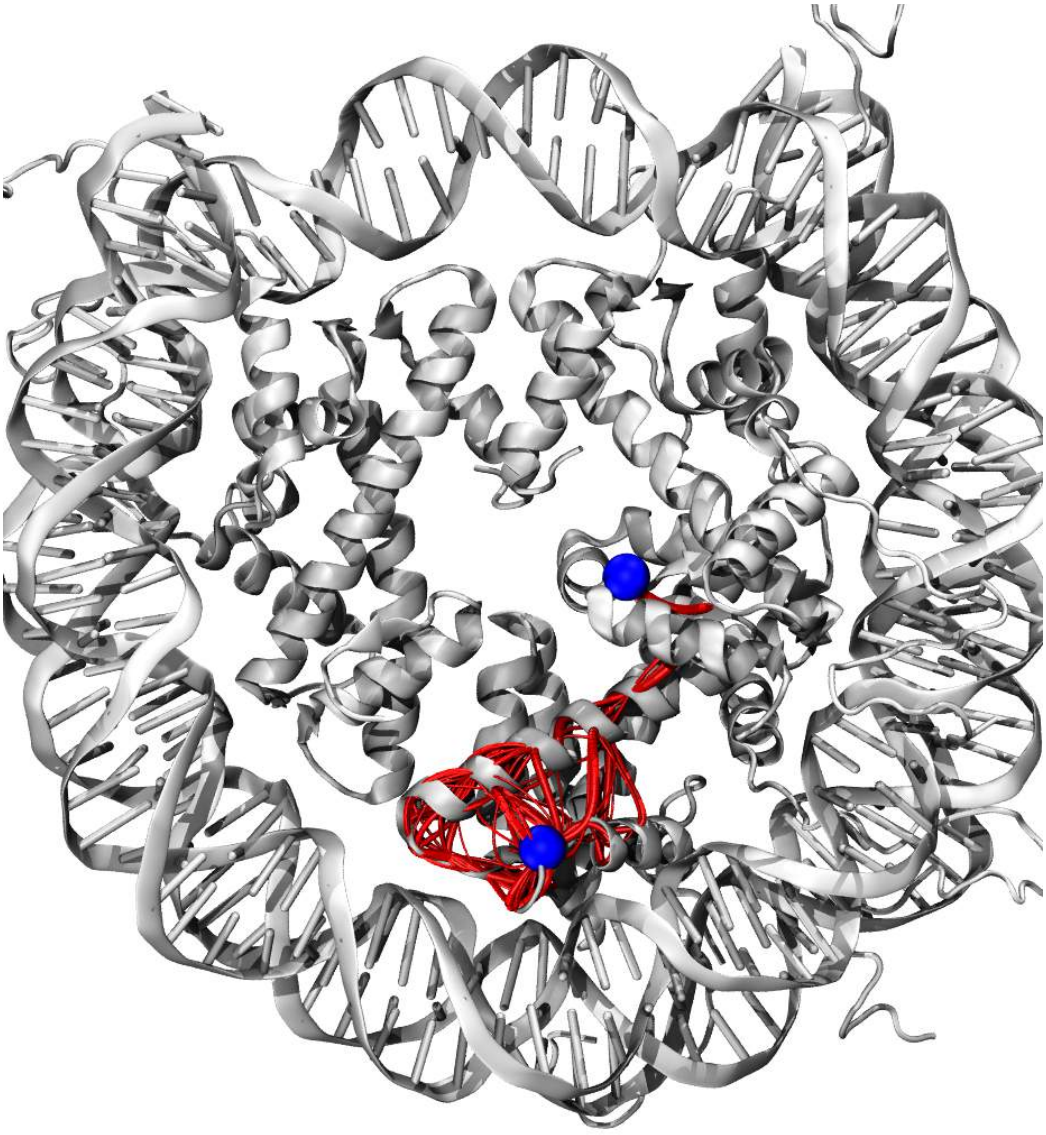

Figure S21: Sub-optimal pathways for L1 loop to the associated docking domain in the H2A.Z nucleosome. The opposing dimer has been removed to improve visualization clarity.

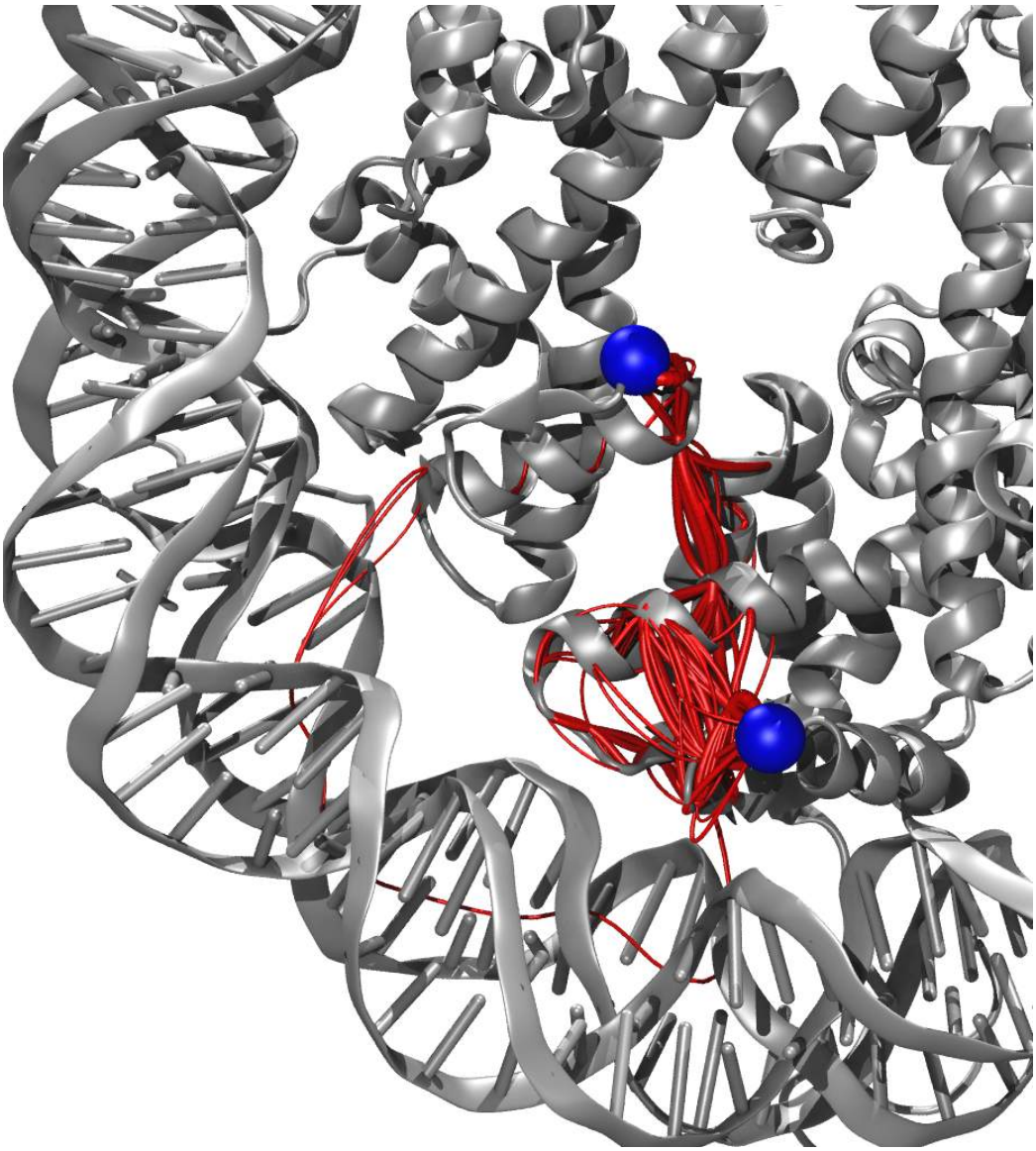

Figure S22: Sub-optimal pathways for L1 loop to non-associated docking domain in the canonical nucleosome. The opposing dimer has been removed to improve visualization clarity.

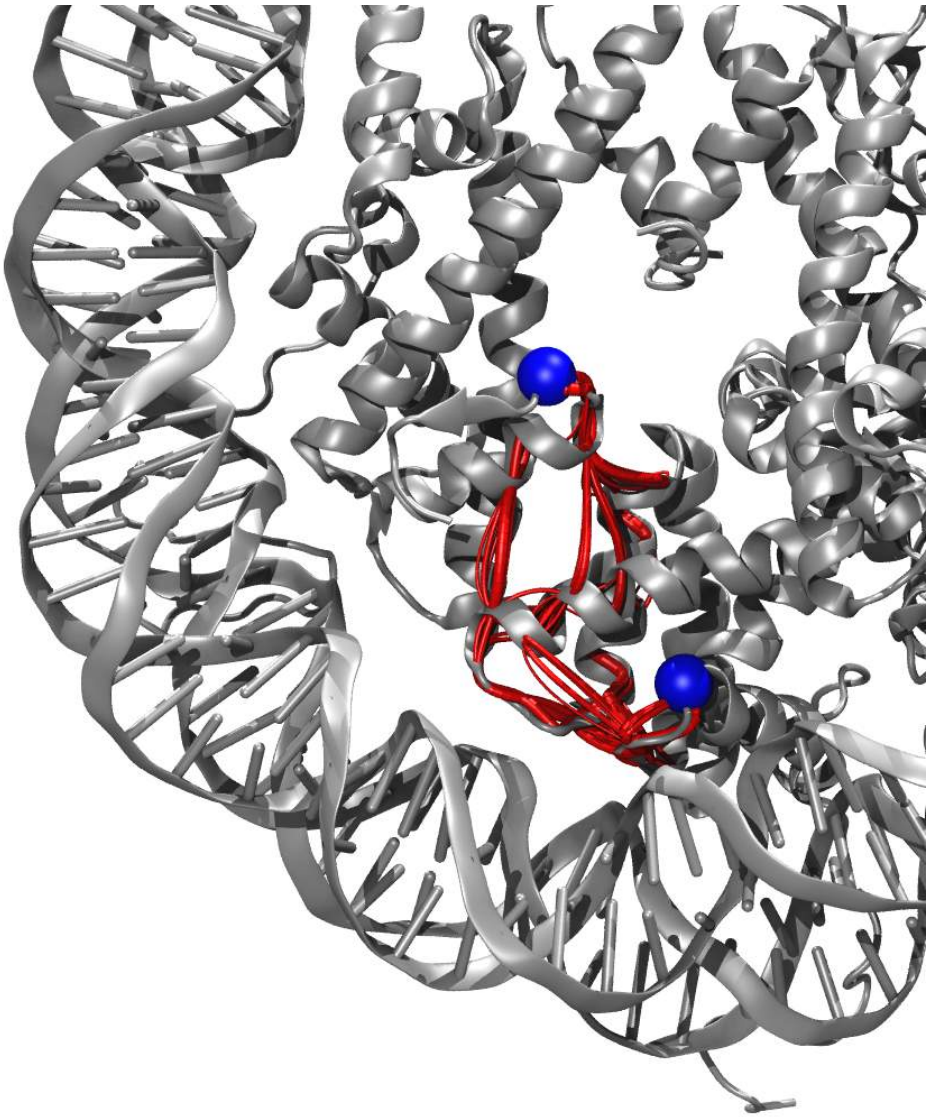

Figure S23: Sub-optimal pathways for L1 loop to non-associated docking domain in the L1-Mutant nucleosome. The opposing dimer has been removed to improve visualization clarity.

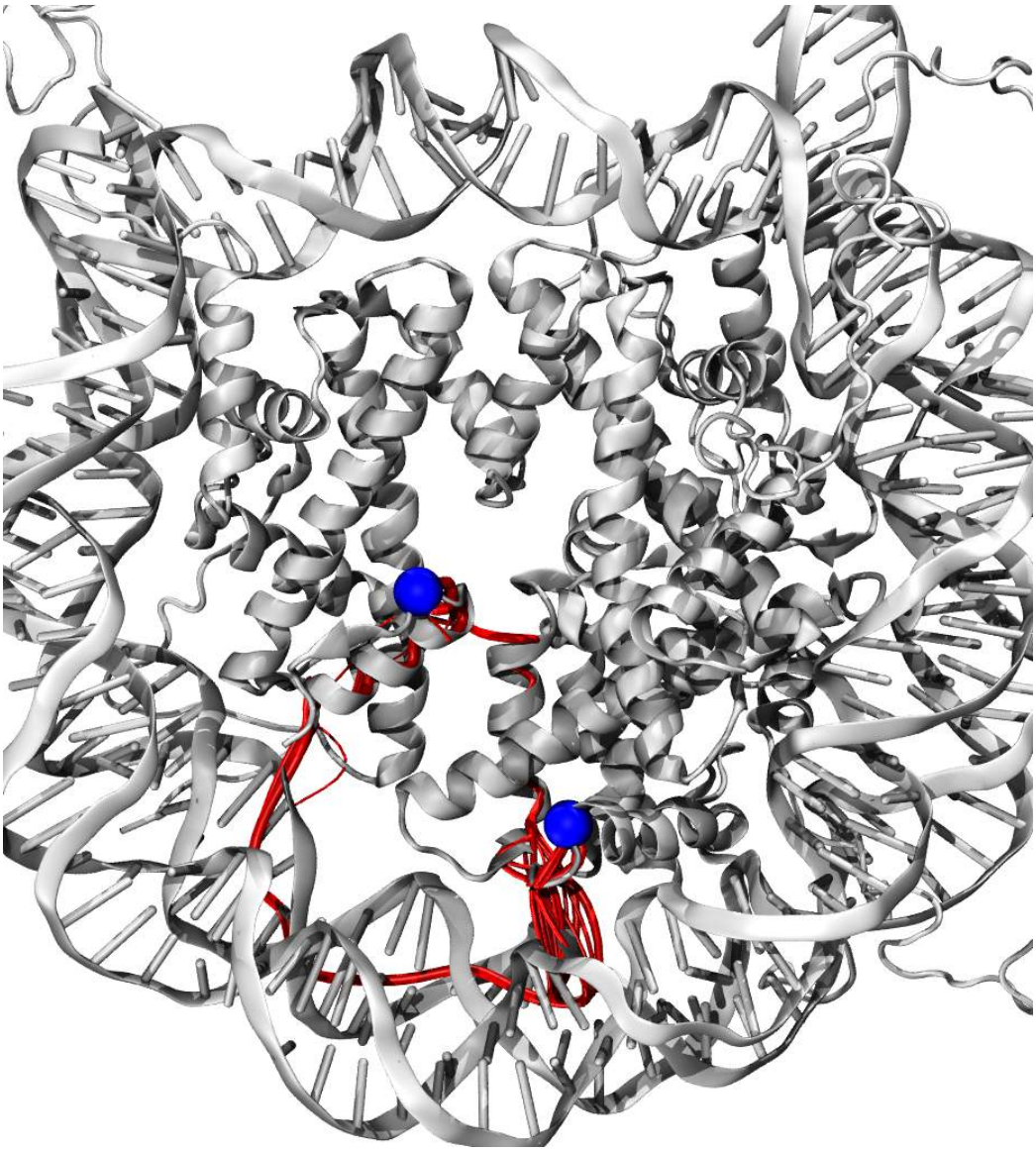

Figure S24: Sub-optimal pathways for L1 loop to non-associated docking domain in the macroH2A nucleosome. The opposing dimer has been removed to improve visualization clarity.

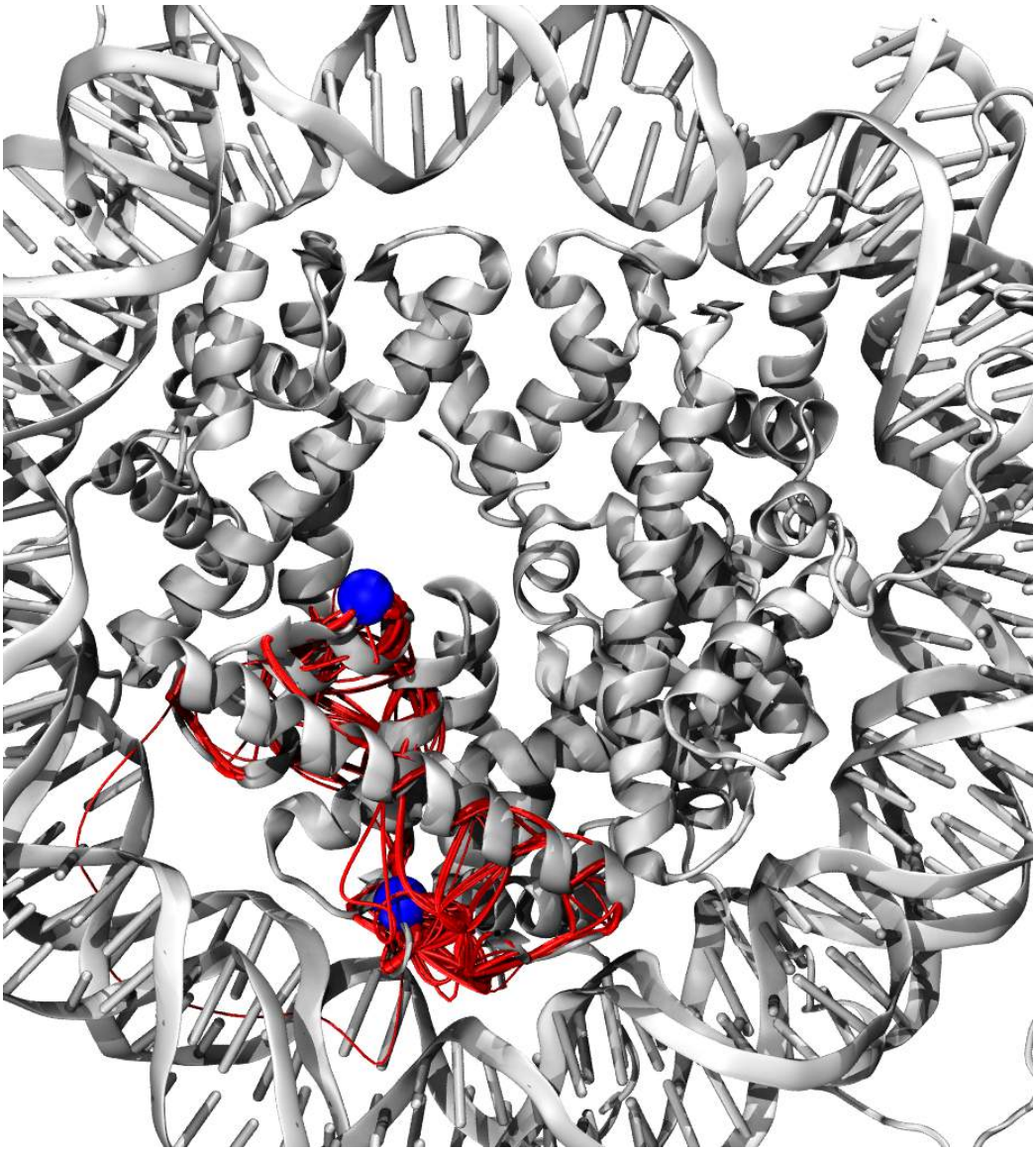

Figure S25: Sub-optimal pathways for L1 loop to non-associated docking domain in the H2A.Z nucleosome. The opposing dimer has been reduced to only H2B α2 to improve visualization clarity.